Mechanical Systems and Signal Processing 158 (2021) 107767

Contents lists available at ScienceDirect

Mechanical Systems and Signal Processing

journal homepage: www.elsevier.com/locate/ymssp

Dynamic analysis of failure paths of truss structures: Benchmark examples including material degradation

Túlio R.C. Felipe [a], André T. Beck [b,*]

[a] *Marinha do Brasil, Diretoria de Obras Civis da Marinha, Rio de Janeiro, RJ, Brazil*

[b] *Department of Structural Engineering – University of São Paulo, Av. Trabalhador São-carlense, 400, 13566-590 São Carlos, SP, Brazil*

A R T I C L E I N F O

Article history:
Received 28 August 2020
Received in revised form 14 February 2021
Accepted 17 February 2021

Communicated by John E. Mottershead

Keywords:
Progressive collapse
Failure paths
Truss structures
Continuum damage mechanics
Dynamic loading

A B S T R A C T

We propose novel benchmark examples of dynamic failure paths of truss structures. Novelty arises from use of a logarithmic strain measure, within a total Lagrangian formulation, combined with a continuum material damage model. Previous benchmarks have considered the usual engineering strain measure, which is not always useful, as it can lead to material degeneration under finite levels of stress. Ductile material behavior has been considered in the literature, addressing plasticity and some material softening, but neglecting material degradation. Herein, damage accumulation is associated to the hydrostatic component of plastic strains, leading to a stable and explicit representation of material degradation. The original static formulation, presented elsewhere by the authors, is extended herein to the dynamic analysis of failure paths of truss structures. Several numerical examples from the literature are studied, and the differences in dynamic behavior are pointed out. In our implementation, as individual bars are damaged, elastic unloading and load redistribution are observed. When the critical damage hypothesized by Lemaitre is reached by individual bars, these are fully unloaded, with no material degeneration or numerical instability. Numerical results highlight the significant effects of material degradation in the dynamic behavior of truss structures under exceptional loads. We propose the set of examples addressed herein as the new benchmarks to which future developments in geometrical and material non-linear truss modelling will be compared.

© 2021 Elsevier Ltd. All rights reserved.

1. Introduction

Recent events leading to partial or full structural collapses such as Ronan Point Tower (UK, 1968) and Skyline Plaza (US, 1973), and terrorist attacks like those at Oklahoma City (1995) and World Trade Center (NY, 9/11, 2001) have raised awareness about the importance of robust design, with objective consideration of progressive collapse following local damage by abnormal loads.

Progressive collapse occurs when structures cannot totally dissipate the kinetic energy of abnormal loads [1–4]. Among the complex energy dissipation mechanisms, there is the plastic work in element deformation, and the energy dissipation associated with structural damping [5]. The response of structures during, or at the brink of progressive collapse, presents a high degree of geometrical and material nonlinear behavior [6,7]. Therefore, material and geometric nonlinearities need to be considered in the dynamic analysis of failure paths.

* Corresponding author.
E-mail address: atbeck@sc.usp.br (A.T. Beck).

https://doi.org/10.1016/j.ymssp.2021.107767
0888-3270/© 2021 Elsevier Ltd. All rights reserved.

As well pointed out by Adams et al. [8], the numerical analysis of failure paths also requires stable and efficient numerical algorithms. Stability, in this context, means that complete failure of individual elements should not cause numerical problems to the solver. Efficiency means that accurate numerical solutions for realistic structures should be obtainable within acceptable computation times.

A number of methods have been presented in the literature to address the nonlinear dynamic modelling of failure paths of truss structures. Nonlinear hysteretic Ramberg-Osgood material models where considered by Noor and Peters [9] and by Zhu et al. [10]. Noor and Peters [9] presented a mixed formulation, involving algebraic and differential equations for unknown member loads and nodal displacements; Zhu et al. [10] employed an updated Lagrangian formulation. Malla et al. [11] developed a FEM model which could track and reproduce the force–deformation characteristics of individual truss members during cyclic loading. A similar idea was developed by Thai and Kim [12], who also implemented a Lagrangian formulation to efficiently handle the large displacements observed in the failure paths. Both studies [11,12] employ the usual engineering strain measure, which can lead to material degeneration, under finite levels of stress. The formulations above [9–12] address ductile non-linear material behavior, and they can capture some material softening, but they don't account for increase in the material yield surface, nor explicitly model material degradation.

A novel formulation is presented herein, for the dynamic analysis of failure paths of truss structures, which explicitly models material degradation, and which accounts for increase in the material yield surface. The work is an extension of the static formulation by Felipe et al. [13], which combines: a total Lagrangian formulation, an objective strain measure, ductile and damage material modelling, with damage described by porosity accumulation. In this manuscript, the static formulation in [13] is extended for the dynamic modelling of truss failure paths. The developed model is usefull in progressive collapse analysis of truss structures, but in this manuscript, only failure path analysis is considered. Yet, failure paths are analyzed until the complete collapse of the truss structure.

The positional FEM approach adopted herein uses simple mathematical formalism and does not require rotation of coordinate systems; this leads to easy numerical implementation and low computational cost. A logarithmic strain measure is employed, leading to a geometrically exact description of the solid deformation. The formulation includes a comprehensive ductile-damage material model, relating the hydrostatic component of plastic strains to accumulated damage and objective material degradation. In Felipe et al. [13], this model is shown to accurately represent the static response of eight different materials, ranging from softening to hardening behavior. In this paper, the formulation is extended to the dynamic analysis of failure paths of truss structures. A number of benchmark problems from the literature is analyzed, ranging from academic to practical application examples. Results demonstrate accuracy and efficiency of the formulation. Results highlight the effects of material degradation in the dynamic behavior of truss structures.

2. A total-Lagrangian formulation for material and geometrical nonlinear dynamic analysis of truss failure paths

2.1. Strain energy and logarithmic strain measure

The total mechanical energy (Π) of a truss structure can be expressed as follows:

$$\Pi = U + K + P + \Lambda \tag{1}$$

where U is the strain energy; K is the kinetic energy; P is the potential energy of the applied forces, and Λ is the dissipated energy.

The strain energy stored in structural elements is defined as [14–16]:

$$U = \int_{V_0} \Psi dV_0 \tag{2}$$

where Ψ is the Helmholtz free energy potential, and V_0 is the initial volume, related to the initial configuration.

One key advantage of the model presented herein, in comparison to the literature [9–12],[1] is use of a logarithmic or true strain measure, $\varepsilon_{ln} = \ln(1+\varepsilon)$. When combined with the Lagrangian formulation, this leads to an exact description of the solids deformation, and avoids material degeneration. When combined with a material damage model, this allows smooth unloading of failed bars, with stability in numerical computations.

Assuming the multiplicative decomposition [17–20] of the logarithmic strain measure $(\varepsilon_{\ln})$, and the decoupling between elasticity-damage and plastic hardening [21], Ψ can be written as follows [13]:

$$\Psi\left(\varepsilon_{\ln}^{e}, D, \varpi\right) = \frac{1}{2}\varepsilon_{\ln}^{e}(1-D)\aleph\varepsilon_{\ln}^{e} + \frac{1}{2}\varpi\Im\varpi \tag{3}$$

where $\varepsilon_{\ln}^{e}$ is the elastic part of log-strain; D is the damage variable; $\aleph$ is the elastic modulus of the undamaged material; $\Im$ is the isotropic hardening parameter, and ϖ is the internal hardening variable.

In classical plasticity formulation, the plastic potential $F(\tau,\chi)$ is defined by [22,23]:

[1] Engineering strain measure ε is employed in [12,13].

$$\dot{\varepsilon}_{\ln}^{p} = \dot{\gamma}\frac{\partial F(\tau,\chi)}{\partial \tau} \text{ and } \dot{\varpi} = \dot{\gamma}\frac{\partial F(\tau,\chi)}{\partial \chi} \tag{4}$$

where the dot $(\dot{})$ denotes temporal derivate; $\varepsilon_{\ln}^{p}$ is the plastic part of log-strain; γ is the plastic multiplier, which must satisfy the classic Kuhn-Tucker relations [22], and χ is the thermodynamic force, which is the conjugate of hardening [24,25], and which is written as:

$$\chi = -\frac{\partial \Psi\left(\varepsilon_{\ln}^{e}, D, \varpi\right)}{\partial \varpi} = -\Im\varpi \tag{5}$$

The minus sign in Eq. (5) denotes that χ is dissipative. In the proposed formulation, $\varepsilon_{\ln}^{p}$ and ϖ are updated using the return mapping algorithm [20]. Moreover, the formulation assumes von Mises yield criterion and multilinear isotropic hardening behavior [13]. Consequently, for the uniaxial case, the yield function $f\left(\tilde{\tau},\chi\right)$ is defined as follows [22]:

$$f\left(\tilde{\tau},\chi\right) = \| \tilde{\tau} \| - (\tau_y + \chi) \tag{6}$$

where τ_y is the initial size of the yield surface; ||.|| is the Euclidian norm, and $\tilde{\tau}$ is the effective stress, defined by [21]:

$$\tilde{\tau} = \frac{\tau}{1-D} = \aleph\varepsilon_{\ln}^{e} = \aleph\left(\varepsilon_{\ln} - \varepsilon_{\ln}^{p}\right) \tag{7}$$

In Eq. (7), $\tau = \frac{\partial \Psi}{\partial \varepsilon_{\ln}}$ is the Kirchhoff stress, which is the conjugate of the log-strain measure.

2.2. Material damage modelling

One key novelty of the model presented herein, in comparison to the literature [9–12], is the explicit modelling of material damage. Material damage is assumed to be caused by micro-void growth and coalescence, or porosity accumulation [13]. The damage evolution law results in a comprehensive ductile-damage model, as proposed in [13]:

$$D(\varphi) = \alpha_1^p\left(\varphi - \varepsilon_{\ln,d}^{p}\right)^2 + \alpha_2^p\left(\varphi - \varepsilon_{\ln,d}^{p}\right) + \alpha_3^p \tag{8}$$

where φ is the plastic extension measure; α_1^p, α_2^p and α_3^p are characteristic parameters of the material, $\varepsilon_{\ln,d}^{p}$ is the initial damage threshold. One important feature of the FLHB model [13] is that the damage variable in Eq. (8) converges to the critical damage value hypothesized by Lemaitre [26]:

$$D_{crit} = 1 - \frac{\tau_r}{\tau_u} \tag{9}$$

where D_{crit} is the critical damage, τ_r is the rupture stress and τ_u is the ultimate stress.

Taking into account the effect of damage, stress in the softening regime is given by:

$$\tau = (1-D)\aleph\varepsilon_{\ln}^{e} = (1-D)\aleph\left(\varepsilon_{\ln} - \varepsilon_{\ln}^{p}\right) \tag{10}$$

Note that the explicit consideration of material damage, and its implementation within a total Lagrangian formulation implementation using nodal positions and a logarithmic strain measure, is the main contribution of ref. [13], which is extended herein to dynamic analysis of failure paths of truss structures. This results in significant extension to the state-of-the-art, in comparison to the relevant work in refs. [11,12]. The logarithmic strain measure provides an exact geometric description of structural behavior, avoids material degeneration under large deformations. Moreover, material hardening and softening are readily captured, as well as material degradation due to porosity accumulation. These modelling advantages are explored in the results section, where benchmark solutions are computed and compared with those of the literature.

2.3. Kinetic energy and damping

The kinetic energy is defined as follows [27–29]:

$$K = \frac{1}{2}\int_{V_0} \rho_0 \dot{\boldsymbol{Z}} \cdot \dot{\boldsymbol{Z}}\, dV_0 \tag{11}$$

where $\dot{\boldsymbol{Z}}$ is the velocity vector, in the current configuration, of a general point inside the domain, and ρ_0 is the mass density related to the initial configuration.

In a mechanical system subject to conservative external forces, the potential energy of the applied forces is defined by [30]:

$$P = -\boldsymbol{F}^{(ext)} \cdot \boldsymbol{Z} \tag{12}$$

where $\mathbf{F}^{(\mathrm{ext})}$ is the applied external force vector, and $\mathbf{Z}$ is the vector of nodal positions in the current configuration.

The dynamic behavior of structures is associated with a process of energy dissipation, generally known as damping [27]. The damping effect can be idealized through an analogy to viscous damping in fluids, as proposed by Newton [28,29]. In the case of viscous damping, energy dissipation Λ is proportional to velocity [31]:

$$\Lambda = \oint \mathbf{F}^{(dam)} \cdot d\mathbf{Z} \tag{13}$$

where $\mathbf{F}^{(dam)}$ is the damping force vector, defined in terms of nodal positions [31]:

$$\mathbf{F}^{(dam)} = \mathbf{C} \cdot \dot{\boldsymbol{Z}} \tag{14}$$

and where $\mathbf{C}$ is the damping matrix. Substituting Eq. (14) in Eq. (13), one obtains:

$$\Lambda = \oint \boldsymbol{C} \cdot \dot{\boldsymbol{Z}} d\boldsymbol{Z} = \oint \boldsymbol{C} \cdot \dot{\boldsymbol{Z}} \left(\frac{d\boldsymbol{Z}}{dt}\right) dt = \oint \boldsymbol{C} \cdot \dot{\boldsymbol{Z}} \cdot \dot{\boldsymbol{Z}} dt. \tag{15}$$

Assuming proportional damping, the damping matrix can be obtained from a Caughey series [32], as follows:

$$\boldsymbol{C} = \boldsymbol{M} \sum_{i=0}^{k-1} \eta_i \left(\mathbf{M}^{-1} \cdot \boldsymbol{H}_0\right)^i \tag{16}$$

where η_i are arbitrary proportionality factors, which must satisfy the conditions of orthogonality [27,28]; $\mathbf{M}$ is a constant mass matrix, and $\mathbf{H}_0$ is the static hessian matrix, evaluated in the initial configuration.

For k = 2, Eq. (16) results in the Rayleigh method [33], which can be rewritten as:

$$\boldsymbol{C} = \eta_0 \boldsymbol{M} + \eta_1 \boldsymbol{H}_0 \tag{17}$$

In this paper, proportional mass damping [34,35] is considered, i.e, η_1 = 0. Consequently, Eq. (17) becomes [27]:

$$\boldsymbol{C} = \eta_0 \boldsymbol{M} = 2\xi\omega \boldsymbol{M} \tag{18}$$

where ξ is the damping ratio, and ω is angular frequency.

A constant mass matrix is considered in the truss formulation, hence:

$$\boldsymbol{M} = \frac{\rho_0 A_0 l_0}{2} \boldsymbol{I} \tag{19}$$

where A_0 is the initial cross-sectional area; l_0 is the initial length of the truss finite element, and $\mathbf{I}$ is the identity matrix.

2.4. Initial, intermediary and current configurations

The proposed formulation is based on three mappings: one related to the initial configuration, one associated with the intermediary configuration, and the third to the current configuration. For the following development, kinematics mapping is adopted, following [13].

2.5. Solution procedure

When written in terms of nodal positions (instead of displacements) [31], the total mechanical energy in Eq. (1) becomes:

$$\Pi(\boldsymbol{Z}) = \int_{V_0} \Psi(\varepsilon_{\ln}(\boldsymbol{Z}), D, \varpi) dV_0 + \frac{1}{2} \int_{V_0} \rho_0 \dot{\boldsymbol{Z}} \cdot \dot{\boldsymbol{Z}} dV_0 + \oint \boldsymbol{F}^{(dam)} \cdot d\boldsymbol{Z} - \boldsymbol{F}^{(ext)} \cdot \boldsymbol{Z}. \tag{20}$$

This functional does not depend on parameters ϖ and D, because of the intrinsic relation between ε_{ln} and τ [13]. The principle of stationarity states that any variation of the energy functional (Eq. (20)) is zero at the equilibrium position, i.e.:

$$\frac{\partial \Pi(\boldsymbol{Z})}{\partial \boldsymbol{Z}} \delta \boldsymbol{Z} = \frac{\partial U}{\partial \boldsymbol{Z}} \delta \boldsymbol{Z} + \frac{\partial K}{\partial \boldsymbol{Z}} \delta \boldsymbol{Z} + \frac{\partial \Lambda}{\partial \boldsymbol{Z}} \delta \boldsymbol{Z} + \frac{\partial P}{\partial \boldsymbol{Z}} \delta \boldsymbol{Z} = \vec{0}. \tag{21}$$

Due to the arbitrariness of $\delta\mathbf{Z}$, Eq. (21) results in n geometrical nonlinear dynamic equilibrium equations.

The strain energy variation concerning nodal positions defines the internal forces vector $\boldsymbol{F}^{(int)}$ [36]. By the energy conjugate principle, the derivative of Helmholtz free energy potential concerning the log-strain measure is the Kirchhoff stress [37]. Thus, by applying the chain rule on the first term of Eq. (21), one obtains:

$$\boldsymbol{F}^{(int)}(\boldsymbol{Z}) = \frac{\partial U}{\partial \boldsymbol{Z}} = \int_{V_0} \frac{\partial \Psi(\varepsilon_{\ln}(\boldsymbol{Z}), D, \varpi)}{\partial \varepsilon_{\ln}} \frac{\partial \varepsilon_{\ln}}{\partial \boldsymbol{Z}} dV_0 = \int_{V_0} \tau \frac{\partial \varepsilon_{\ln}}{\partial \boldsymbol{Z}} dV_0 \tag{22}$$

where

$$\frac{\partial \varepsilon_{\ln}}{\partial Z_i^\alpha} = (-1)^\alpha \frac{\left(z_i^2 - z_i^1\right)}{l^2}. \tag{23}$$

In Eq. (23), parameters $\alpha = 1, 2$ represent finite element nodes; $i = 1, 2$ or $i = 1, 2, 3$ indicates axes direction, for truss finite elements in 2D and 3D, respectively; l is the element length in the current configuration, and z are the current coordinates of the nodes.

By the d'Alembert's principle, the kinetic energy variation results in the inertia force vector $\mathbf{F}^{(\mathrm{ine})}$, according to [27]:

$$\boldsymbol{F}^{(ine)}\left(\ddot{\boldsymbol{Z}}\right) = \boldsymbol{M} \cdot \ddot{\boldsymbol{Z}}. \tag{24}$$

The dissipation energy variation results in the damping force vector $\mathbf{F}^{(\mathrm{dam})}$ [27], according to Eq. (14).

For conservative forces, the potential energy variation of the applied forces results in the applied external force vector $\mathbf{F}^{(\mathrm{ext})}$ [30], according to Eq. (12). Substituting Eqs. (22) and (24) in (21), leads to the following:

$$\vec{\Re}(\boldsymbol{Z}) = \boldsymbol{F}^{(int)}(\boldsymbol{Z}) + \boldsymbol{F}^{(\mathrm{ine})}\left(\ddot{\boldsymbol{Z}}\right) + \boldsymbol{F}^{(\mathrm{dam})}\left(\dot{\boldsymbol{Z}}\right) - \boldsymbol{F}^{(\mathrm{ext})} = \vec{0} \tag{25}$$

where $\vec{\Re}$ is the unbalanced force vector [16], which is a function of the current position vector $\mathbf{Z}$.

Evaluation of Eq. (25) requires an algorithm for the integration in time. Therefore, Eq. (25) is first written in terms of time steps t_{s+1}, as follows:

$$\vec{\Re}(\boldsymbol{Z}_{s+1}) = \boldsymbol{F}^{(int)}(\boldsymbol{Z}_{s+1}) + \boldsymbol{F}^{(\mathrm{ine})}\left(\ddot{\boldsymbol{Z}}_{s+1}\right) + \boldsymbol{F}^{(\mathrm{dam})}\left(\dot{\boldsymbol{Z}}_{s+1}\right) - \boldsymbol{F}^{(\mathrm{ext})}_{s+1} = \vec{0}. \tag{26}$$

To solve Eq. (26), the Newmark time integration [38] and the Newton-Raphson algorithms have been combined. Then, Newmark's approximations, written concerning nodal positions, can be written as follows [16]:

$$\dot{\boldsymbol{Z}}_{s+1} = \boldsymbol{R}_s - \gamma_n \Delta t \boldsymbol{Q}_s + \frac{\gamma_n \boldsymbol{Z}_{s+1}}{\beta_n \Delta t} \tag{27}$$

$$\ddot{\boldsymbol{Z}}_{s+1} = \frac{\boldsymbol{Z}_{s+1}}{\beta_n \Delta t^2} - \boldsymbol{Q}_s \tag{28}$$

where,

$$\boldsymbol{Q}_s = \frac{\boldsymbol{Z}_s}{\beta_n \Delta t^2} + \frac{\dot{\boldsymbol{Z}}_s}{\beta_n \Delta t} + \left(\frac{1}{2\beta_n} - 1\right)\ddot{\boldsymbol{Z}}_s \tag{29}$$

$$\boldsymbol{R}_s = \dot{\boldsymbol{Z}}_s + \Delta t(1 - \gamma_n)\ddot{\boldsymbol{Z}}_s. \tag{30}$$

In Eqs. (27) to (30), β_n and γ_n are the usual Newmark parameters [28]; Δt is time step, and $\mathbf{Q}_s$ and $\mathbf{R}_s$ denote the dynamic contribution of the past [16].

Substituting Eqs. (27) and (28) in (26), and recalling Eqs. (14) and (24), leads to the following:

$$\vec{\Re}(\boldsymbol{Z}_{s+1}) = \boldsymbol{F}^{(int)}(\boldsymbol{Z}_{s+1}) + \frac{\boldsymbol{M} \cdot \boldsymbol{Z}_{s+1}}{\beta_n \Delta t^2} - \boldsymbol{M} \cdot \boldsymbol{Q}_s + \frac{\gamma_n \boldsymbol{C} \cdot \boldsymbol{Z}_{s+1}}{\beta_n \Delta t} + \boldsymbol{C} \cdot \boldsymbol{R}_s - \gamma_n \Delta t \boldsymbol{C} \cdot \boldsymbol{Q}_s - \boldsymbol{F}^{(\mathrm{ext})}_{s+1} = \vec{0} \tag{31}$$

The Taylor series expansion of Eq. (31) for trial position $\boldsymbol{Z}^0_{s+1}$ results in:

$$\vec{\Re}(\boldsymbol{Z}_{s+1}) \cong \vec{\Re}\left(\boldsymbol{Z}^0_{s+1}\right) + \nabla\vec{\Re}\left(\boldsymbol{Z}^0_{s+1}\right) \cdot \Delta\boldsymbol{Z}_{s+1} = \vec{\Re}\left(\boldsymbol{Z}^0_{s+1}\right) + \boldsymbol{H} \cdot \Delta\boldsymbol{Z}_{s+1} = \vec{0} \tag{32}$$

where $\mathbf{H}$ is the Hessian matrix. Since Eq. (32) is nonlinear, the Newton-Raphson algorithm is applied, leading to the following:

$$\Delta\boldsymbol{Z}_{s+1} = -\boldsymbol{H}^{-1} \cdot \vec{\Re}\left(\boldsymbol{Z}^0_{s+1}\right). \tag{33}$$

Consequently, a new trial position is calculated by:

$$\boldsymbol{Z}_{s+1} = \boldsymbol{Z}^0_{s+1} + \Delta\boldsymbol{Z}_{s+1}. \tag{34}$$

The velocity and acceleration are corrected by Eqs. (27) and (28), respectively. The iterative process occurs until the following stopping criteria are satisfied:

$$\frac{\| \vec{\Re}(\boldsymbol{Z}_{s+1}) \|}{\| \boldsymbol{F}^{(ext)} \|} \leqslant \text{tolerance or } \frac{\| \Delta\boldsymbol{Z}_{s+1} \|}{\| \boldsymbol{X} \|} \leqslant \text{tolerance} \tag{35}$$

where $\mathbf{X}$ is the initial position vector.

Application of the chain rule on the first term of Eq. (31) leads to the Hessian matrix, which is obtained as follows:

$$\boldsymbol{H} = \nabla \vec{\Re}\left(\boldsymbol{Z}_{s+1}^{0}\right) = \int_{V_0}\left(\frac{\partial \varepsilon_{\ln}}{\partial \boldsymbol{Z}} : \frac{\partial^2 \Psi}{\partial^2 \varepsilon_{\ln}} : \frac{\partial \varepsilon_{\ln}}{\partial \boldsymbol{Z}} + \frac{\partial \Psi}{\partial \varepsilon_{\ln}} : \frac{\partial^2 \varepsilon_{\ln}}{\partial \boldsymbol{Z} \otimes \partial \boldsymbol{Z}}\right) dV_0 + \frac{\boldsymbol{M}}{\beta_n \Delta t^2} + \frac{\gamma_n \boldsymbol{C}}{\beta_n \Delta t}. \tag{36}$$

The first term in Eq. (36) is the static Hessian matrix $\mathbf{H}^{(\mathrm{sta})}$, which can be written as follows:

$$\boldsymbol{H}^{(\mathrm{sta})} = \frac{\partial U}{\partial \boldsymbol{Z} \otimes \partial \boldsymbol{Z}} = \int_{V_0}\left(\frac{\partial \varepsilon_{\ln}}{\partial \boldsymbol{Z}} : \frac{\partial^2 \Psi}{\partial^2 \varepsilon_{\ln}} : \frac{\partial \varepsilon_{\ln}}{\partial \boldsymbol{Z}} + \frac{\partial \Psi}{\partial \varepsilon_{\ln}} : \frac{\partial^2 \varepsilon_{\ln}}{\partial \boldsymbol{Z} \otimes \partial \boldsymbol{Z}}\right) dV_0. \tag{37}$$

The static Hessian matrix for a truss finite element j is given by:

$$\left(H_{hi}^{\alpha\kappa}\right)^j = \frac{A_0^{(j)} l_0^{(j)} (-1)^{\alpha} (-1)^{\kappa}}{l^4}\left\{\aleph_t^j \left(z_h^2 - z_h^1\right)\left(z_i^2 - z_i^1\right) + \tau^j\left[l^2 - 2\left(z_{(h)}^2 - z_{(h)}^1\right)\right]\delta_{hi}\right\} \tag{38}$$

where α = 1, 2 and κ = 1, 2 are the element nodes; i = 1, 2 and h = 1, 2; or i = 1, 2, 3 and h = 1, 2, 3 are the axial directions for truss structures in 2D and 3D, respectively; δ_{hi} is the Kronecker delta, and $\aleph_t$ is the tangent modulus, which is given by the second derivative of the Helmholtz free energy potential [37], as follows:

$$\aleph_t = \frac{\partial \Psi}{\partial^2 \varepsilon_{\ln}}. \tag{39}$$

The comprehensive ductile damage model presented in this section is referenced as FLHB, using the surname initials of the four authors of reference [13]. In ref. [13], the model was implemented for static analysis only; the extension to dynamic analysis is a contribution of this manuscript.

3. Validation: dynamic problems from the literature

3.1. Academic problem with analytic solution

In this section, accuracy of the proposed formulation is demonstrated, in application to an academic problem with analytical solutions: a single bar subject to normal loading. The analysis is performed with and without damping. In the following numerical analysis, a convergence tolerance of 10^{-6} is considered, based on the norm of position changes (Eq. (35)).

Fig. 1(a) presents the geometric input data of the single bar. Cross-section area, bar length, density and damping ratio are given by A_0 = 0.00785 m^2; l_0 = 1 m; ρ_0 = 7850 Kg/m^3 and ξ = 0.1, in that order. Newmark parameters are β_n = 0.25 and γ_n = 0.50. Time step is Δt = 0.025 s. Fig. 1(d) presents the constitutive law of material, where young's modulus and yield stress are given as $\aleph$ = 205000 N/m^2 and σ_y = 250 N/m^2, respectively. Damage parameters are:$\alpha_1^p = 0$; $\alpha_2^p = 11.65$; $\alpha_3^p = 0$; $\varepsilon_{\ln,d}^p = 0.0125$ and D_{crit} = 0.214.

3.1.1. Response to step load

A step load is a discontinuous force that suddenly changes from zero to a constant value f_0 [27], as illustrated in Fig. 1(b). The step load is defined as:

$$F(t) = \begin{cases} f_0 \text{ for t} \geqslant 0 \\ 0 \text{ for t} < 0. \end{cases} \tag{40}$$

The equation of motion of the truss in Fig. 1(a) can be written as:

$$m\ddot{u}(t) + c\dot{u}(t) + ku(t) = F(t) \tag{41}$$

where m is the mass, c is the viscous damping, k is the stiffness, $\ddot{u}(t)$ is the acceleration, $\dot{u}(t)$ is the velocity, $u(t)$ is the displacement, and $F(t)$ is the external force.

Eq. (41) is a nonhomogeneous ordinary differential equation. Thus, the solution $u(t)$ is the sum of the complementary solution (homogeneous equation) and a particular solution (nonhomogeneous equation). In case of an undamped system, with initial conditions $u(0) = \dot{u}(0) = 0$ and $F(t) = f_0$, the displacements are obtained as:

$$u(t) = \frac{f_0}{k}\left[1 - \cos(\omega_n t)\right] \tag{42}$$

where $\omega_n = \sqrt{\frac{k}{m}}$ is the natural angular frequency.

For a dissipative system, with initial conditions $u(0) = \dot{u}(0) = 0$ and F(t) = f_0, the solution of Eq. (41) is expressed as:

$$u(t) = \frac{f_0}{k}\left\{1 - e^{-\xi\omega_n t}\left[\cos(\omega_d t) + \frac{\xi\omega_n}{\omega_d}\sin(\omega_d t)\right]\right\} \tag{43}$$

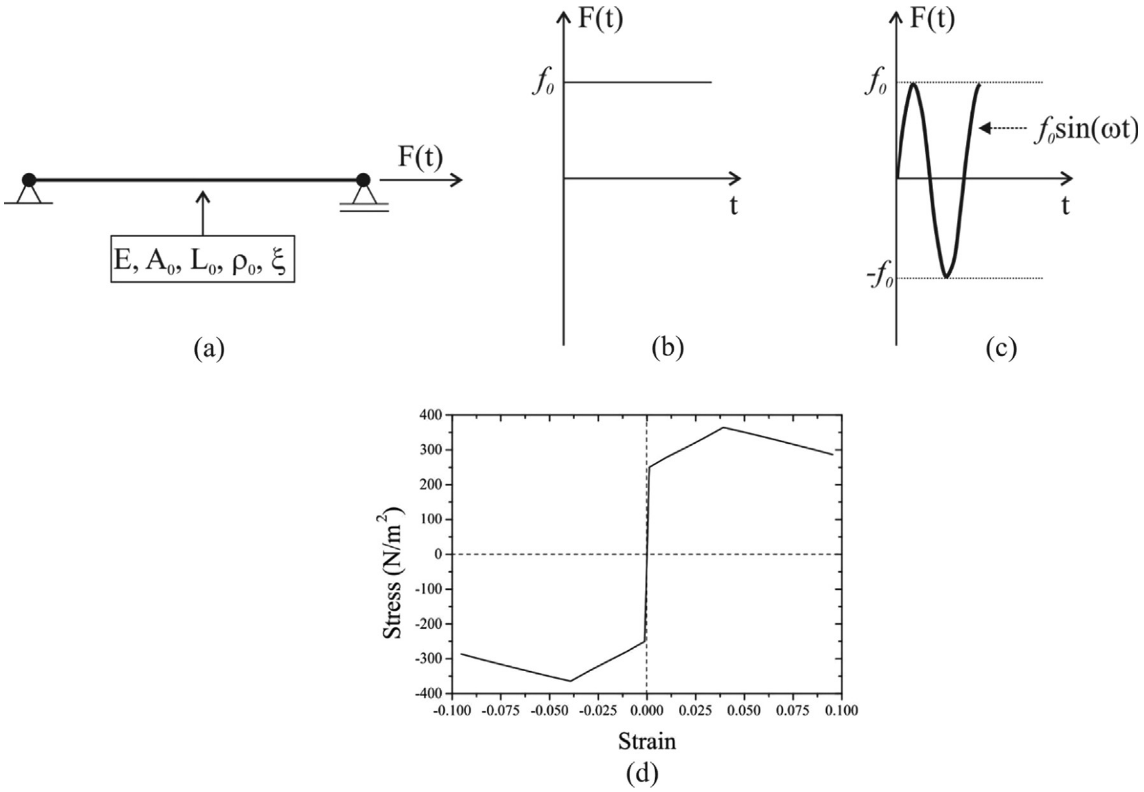

Fig. 1. Input data for academic test problem: (a) geometry; (b) step load; (c) harmonic load; and (d) constitutive law of the material.

where $\omega_d = \omega_n\sqrt{1-\xi^2}$is the dampened vibration frequency and ξ is the damping ratio. With the input data presented above, the system constants become: k = 1609.250 N/m; m = 30.811 Kg; ω_n = 7.227 Hz; and ω_d = 7.191 Hz. The amplitude of external force is assumed equal to f_0 = 5 N.

Fig. 2 compares the analytical response with the respose obtained using the developed formulation. As observed, the solutions are nearly identical. The static displacement is $u_{static} = \frac{f_0}{k} = 0.0031$ m. Note that the dynamic response vibrates around the static response, as expected. In this example, the geometrical nonlinear dynamic solution is approximately equal to the analytic solution, since the level of strains is small.

The Dynamic Amplificatory Factor (*DAF*) for a conservative system is defined as $DAF = 1 - \cos(\omega_n t)$. This equation shows that maximum displacement (u_{max}) of a conservative Single Degree of Freedom (SDOF) system, when a load is suddenly applied, is equal to $u_{max} = 2u_{static}$; a result widely known for undamped systems. For the damped system (Fig. 2(b)), the *DAF* is smaller than 2, due to energy dissipation before the point of maximum amplitude is reached. The first time that u_{max} occurs is calculated by deriving Eq. (43) w.r.t. time and equating to zero, which results in $t_{\max} = \frac{\pi}{\omega_d} = 0.437$ s. At time $t = t_{max}$, the truss reaches u_{max} = 0.0062 m (conservative system) and u_{max} = 0.00536 m (dissipative system), as illustrated in Fig. 2. Consequently, the dissipative system leads a *DAF* equal to 1.73.

Fig. 3 shows the displacement time histories, for the conservative and dissipative systems, when geometrical and material nonlinearities are considered. The analysis is performed considering plasticity, and the comprehensive ductile-damage FLHB model. The constitutive law presented in Fig. 1(d) is used. Fig. 4 illustrates the corresponding stress–strain curves.

As can be observed, in the nonlinear plastic dynamic solution, the element starts yielding under constant stress, as the material ultimate stress is reached. The plastic analysis cannot model softening, which preceeds rupture. On the other hand, the nonlinear dynamic solution using the ductile-damage FLHB model produces very consistent results: the bar softens after reaching the ultimate stress, accumulating damage, and fails when the critical damage value is reached.

The FLHB solution very closely follows the material constitutive law, as illustrated in Fig. 4. When the bar reaches the initial damage threshold, the mechanical degradation process starts, and proceeds until critical damage is reached, leading to failure at t = 1.45 s (displacement = 0.102 m). It is also observed in Fig. 4 that the conservative system is more critical than the dissipative system, since the former presents no energy dissipation. Consequently, the displacements are greater in the undamped system, which leads to an increase in the level of strains, until the bar reaches the critical damage, according to Fig. 5. In contrast, the dissipative system does not reach critical damage. Hence, the energy provided by the external step

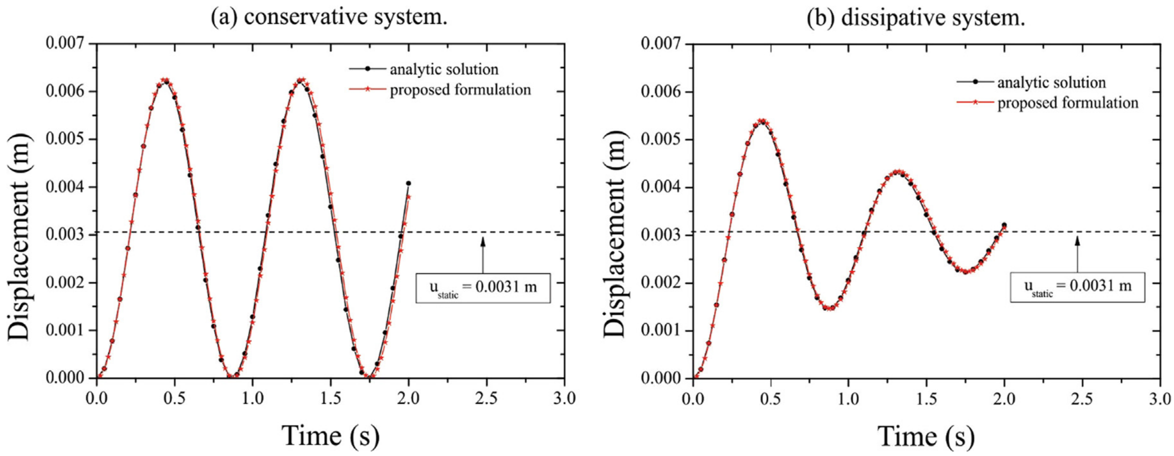

Fig. 2. Displacement time histories considering geometrical nonlinearities only: (a) conservative system and (b) dissipative system.

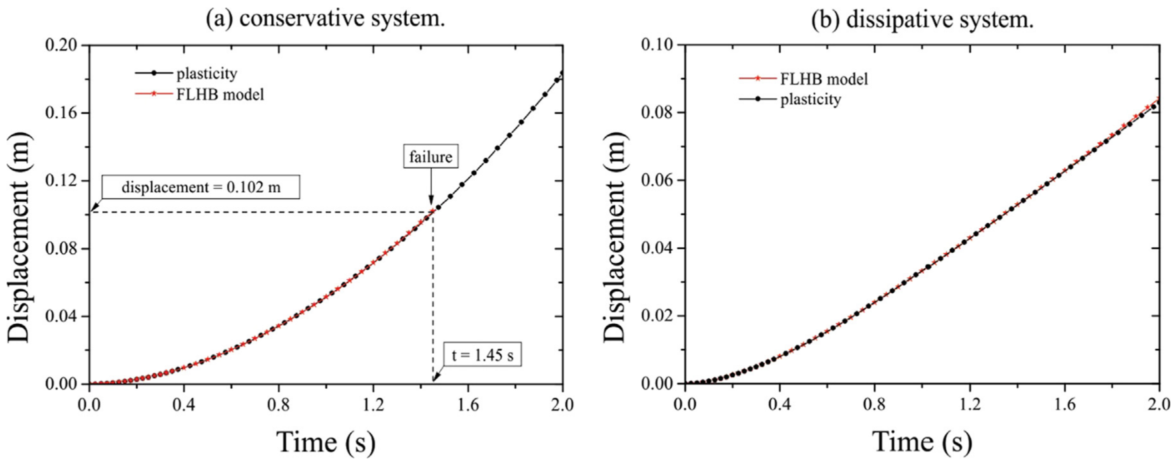

Fig. 3. Displacement time histories considering geometrical and material nonlinearity: (a) conservative system and (b) dissipative system.

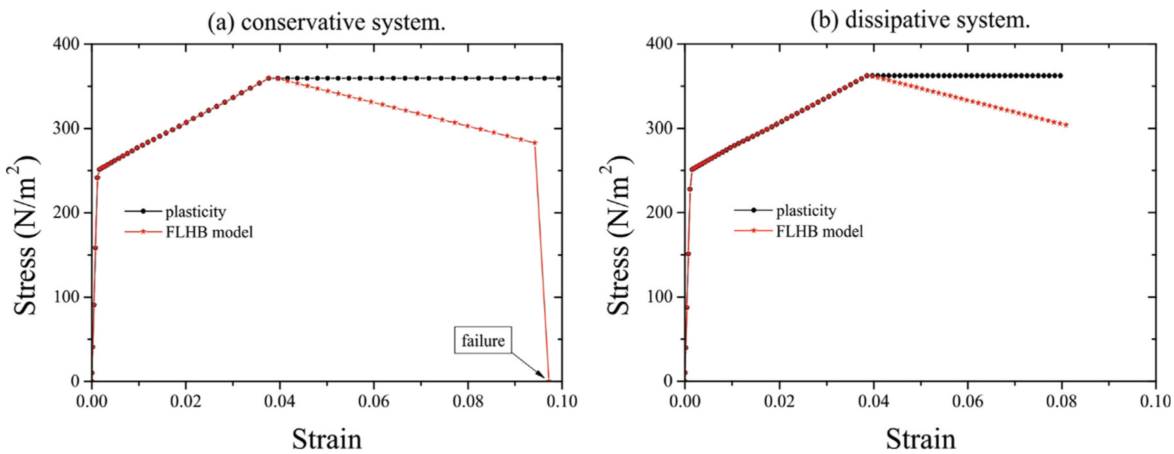

Fig. 4. Stress versus strain in bar: (a) conservative system and (b) dissipative system.

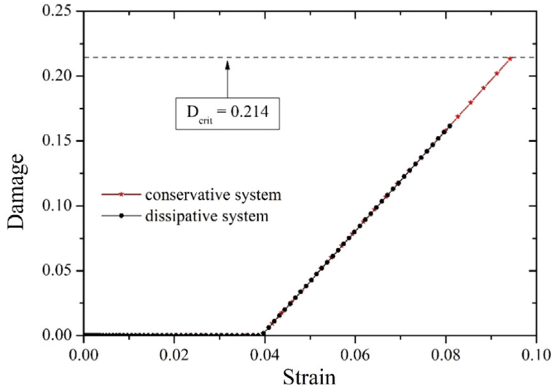

Fig. 5. Damage evolution in bar.

loading considered is sufficient to lead the conservative system to failure, but not the dissipative system. This points to the importance of considering the appropriate energy dissipation mechanisms in numerical analysis of failure paths.

3.1.2. Response to forced harmonic loading

Harmonic loading is a continuous force that usually varies as a sinusoid [27]. Thus, the solution of Eq. (41) for an undamped system, with initial conditions $u(0) = \dot{u}(0) = 0$ and $F(t) = f_0 sin(\omega t)$ becomes:

$$u(t) = \frac{f_0}{k(1-\beta^2)}[\sin(\omega t) - \beta\sin(\omega_n t)] \tag{44}$$

where $\beta = \frac{\omega}{\omega_n}$ is the frequency ratio, $\omega_n = \sqrt{\frac{k}{m}}$ is the natural angular frequency, f_0 is the amplitude of external force (Fig. 1(b)) and ω is the angular frequency of external force, or forcing frequency.

The solution of Eq. (41) for damped system, with initial conditions $u(0) = \dot{u}(0) = 0$ and $F(t) = f_0 sin(\omega t)$ is given by:

$$u(t) = e^{-\xi\omega_n t}[C_1\cos(\omega_d t) + C_2\sin(\omega_d t)] + \ + \frac{f_0}{k\left[\left(1-\beta^2\right)^2 + (2\xi\beta)^2\right]}\left[(1-\beta^2)\sin(\omega t) - 2\xi\beta\cos(\omega t)\right] \tag{45}$$

with

$$C_1 = \frac{2\xi\beta f_0}{k\left[\left(1-\beta^2\right)^2 + (2\xi\beta)^2\right]}$$

$$C_2 = \frac{\omega_n f_0}{k\omega_d}\left[\frac{2\xi^2\beta - \beta\left(1-\beta^2\right)}{\left(1-\beta^2\right)^2 + (2\xi\beta)^2}\right]$$

Fig. 6 shows the displacement time history for the single-bar of Fig. 1(a), subjected to a harmonic force. The external force angular frequency is 6.20 Hz, which is close to the damped and undamped natural frequencies of the system. Remark the excellent agreement of the analytic and numeric responses for the solution with elastic material, for both conservative and dissipative systems. The plastic solution deviates significantly from the elastic: due to accumulated deformation in tensile loading, the plastic solution oscilates around a positive accumulated deformation. The displacements are greater in the conservative system, compared to the dissipative system. Due to damping and plastic strains, energy dissipation in the later leads to smaller displacements in the bar. Remark that the plastic solution for the conservative system is always positive.

Fig. 7(a)–(b) show the nonlinear dynamic response of the bar under harmonic loading. Note that the result obtained for the elastic material is in good agreement with the analytic solution. As observed, the conservative system leads to greater displacements, in both tensile and compression loading. Consequently, the level of strains in the bar is greater in the undamped system, compared to the damped system. As observed in Fig. 7(c), the stress vs. strain curves for the plastic material forms the expected hysteresis loops. This specific area within the loops is proportional to the energy dissipated per cycle [27], in plastic deformations. For the elastic material, the stress vs. strain "loops" degenerate into a straight line. Thus, dissipated energy due to hysteresis loops is equal to zero, according to Fig. 7(c). In this example, the damage response is equal to the plastic response, since the material does not reach the softening regime, as illustrated in Fig. 7(c).

3.2. Numerical solutions

3.2.1. Two-bay cantilever truss

Fig. 8(a) shows a two-bay cantilever plane truss under step load. This truss was studied by Noor & Peters [9] using a mixed formulation, and by Zhu et al. [10] employing an updated Lagrangian formulation. Young's modulus, yield stress, and density

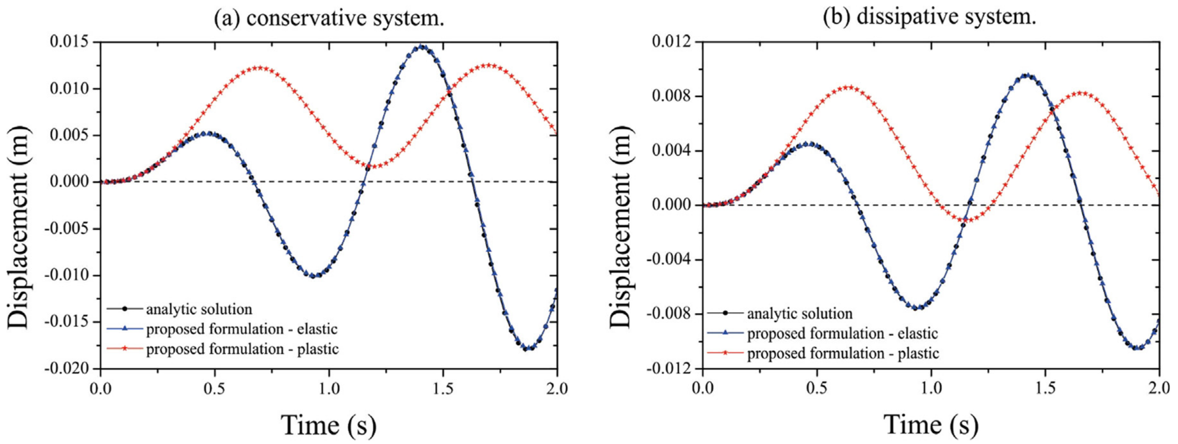

Fig. 6. Displacement time history under harmonic loading: (a) conservative system and (b) dissipative system.

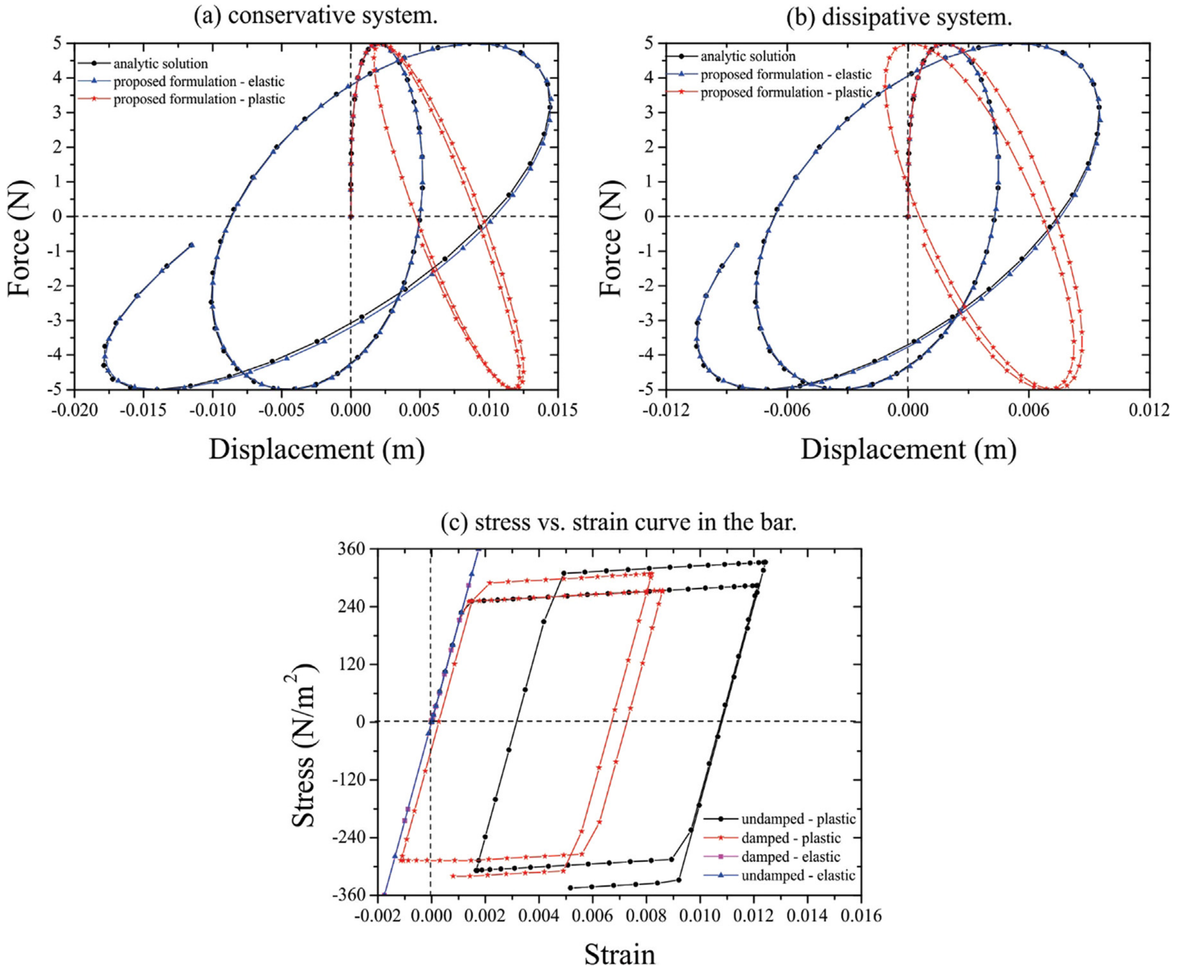

Fig. 7. Nonlinear dynamic response to harmonic loading: (a) force vs. displacement curve for the conservative system; (b) force vs. displacement curve for the dissipative system and (c) stress vs. strain curve of the bar material.

are given as $\aleph$ = 71.7 GPa, σ_y = 280 MPa and ρ_0 = 2768 Kg/m^3. Cross-section area of the horizontal bars is A_h = 160 mm^2, whereas vertical and diagonal bars is A_v = 130 mm^2. Newmark parameters are β_n = 0.25 and γ_n = 0.50. Time step is $\Delta t = 1.474 \times 10^{-4}$ s. Angular natural frequency is 745.9145 Hz. Fig. 8(b) presents the step load, where $f_0 = 4.5 \times 10^4$ N.

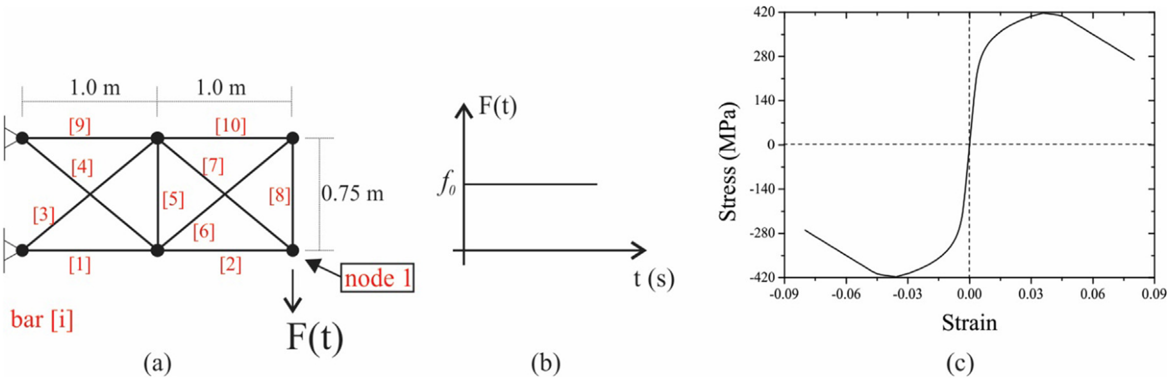

Fig. 8. Input data: (a) geometry of a two-bay cantilever truss; (b) step load; and (c) constitutive law of the material.

Fig. 8(c) presents the constitutive law of the material, for which damage parameters are obtained as: $\alpha_1^p = 612.59$; $\alpha_2^p = 16.956$; $\alpha_3^p = -0.02$;$\varepsilon_{\ln,d}^p = 0.01$ and D_{crit} = 0.354.

Figs. 9 and 10 present the nonlinear dynamic response of the two-bay cantilever plane truss under a step load. Remark that the results obtained are in good agreement with Noor & Peters [9] and Zhu et al. [10]. Note that the plastic and elastic responses are distinctly different. Vertical displacements are greater for the plastic and damage analysis, as illustrated in Fig. 9. On the other hand, normal forces are smaller for plastic and damage analysis, according to Fig. 10.

The proposed formulation achieved solution for each load step with only two and four iterations, respectively, for the elastic and plastic solution. Thus, the proposed formulation, written in terms of nodal positions, presents good accuracy and efficient convergence for dynamic analysis taking into account material and geometrical nonlinearities.

Fig. 11 illustrates the stress–strain response of bars 1 and 9, and the mechanical degradation process for these bars. As observed in Fig. 11(b), the mechanical degradation process of bar 9 is initiated at about t = 0.0042 s, as this bar reaches the initial damage threshold. This leads to a reduction in the level of the stress, and consequently, of the normal force in bar 9, as illustrated in Fig. 10(b). Mechanical degradation of bar 1 starts at about t = 0.0046 s. Damage accumulates in both bars, until critical damage is reached, at t = 0.0066 s and t = 0.0070 s, respectivelly. This leads to the local failure of bars 1 and 9; however, bars 3 and 4 still warrant equilibrium for the two-bay cantilever plane truss under the step load. As noted, the formulations of Noor & Peters [9] and Zhu et al. [10] do not adequately address the response of this structure for times greater that 0.0042 s, as these formulations do not take into account the mechanical degradation process.

3.2.2. Shallow truss arch

Fig. 12(a) presents a shallow truss arch. The geometric input data for this truss is given in ref. [10]; however, the material model we employ is different, as shown in Fig. 12 (c). Cross-section area, density and damping ratio are give A_0 = 0.0154 m^2; ρ_0 = 7850 Kg/m^3 and ξ = 0.1, respectively. Fig. 12(b) illustrates the harmonic loading that is applied in node 1, with parameters f_0 = -1.4x10^5 N and ω = 5 Hz. Fig. 12(c) presents the constitutive law of the material, where young's modulus and yield stress are E_0 = 200 GPa and σ_y = 200 MPa. Material damage parameters are obtained as:$\alpha_1^p = 0$; $\alpha_2^p = 1500$; $\alpha_3^p = 0$;

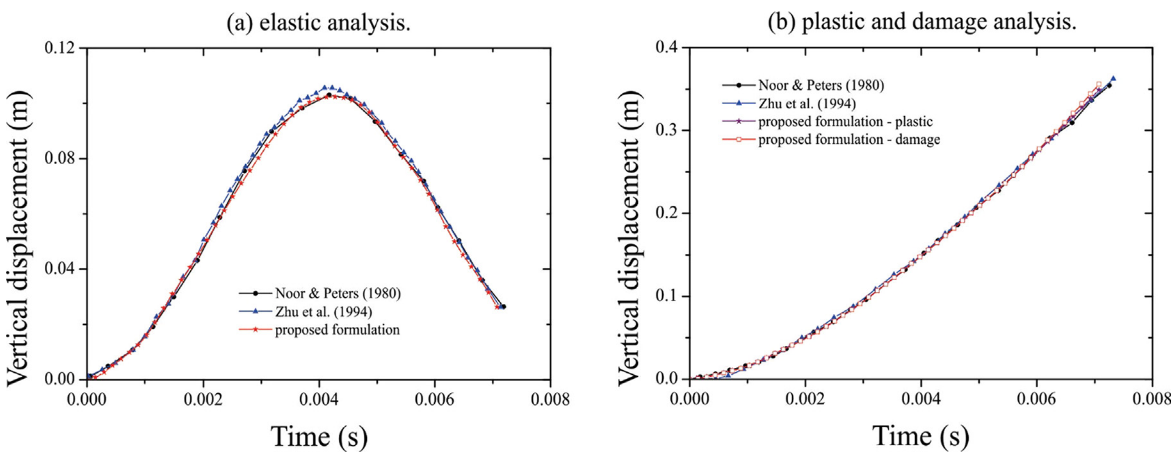

Fig. 9. Displacement time history in node 1: (a) elastic analysis; and (b) plastic and damage analysis.

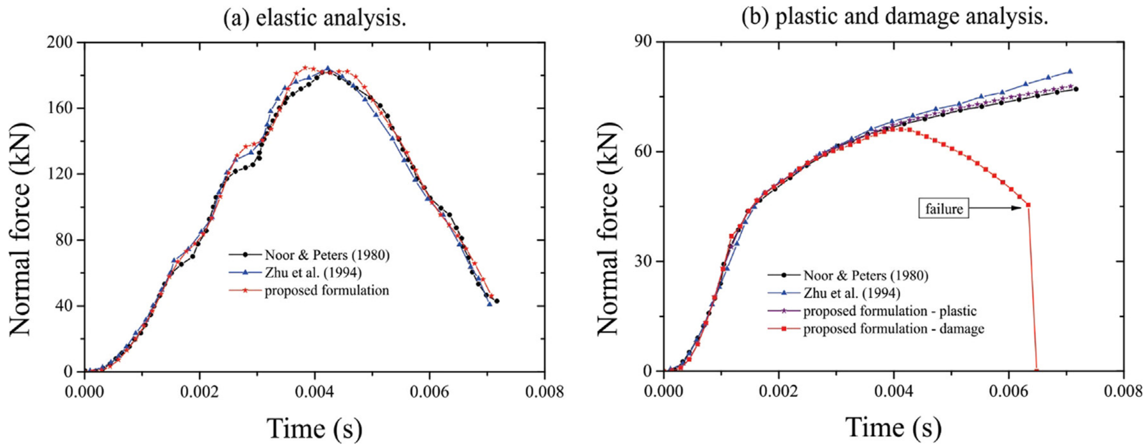

Fig. 10. Normal force in bar 1: (a) elastic analysis; and (b) plastic and damage analysis.

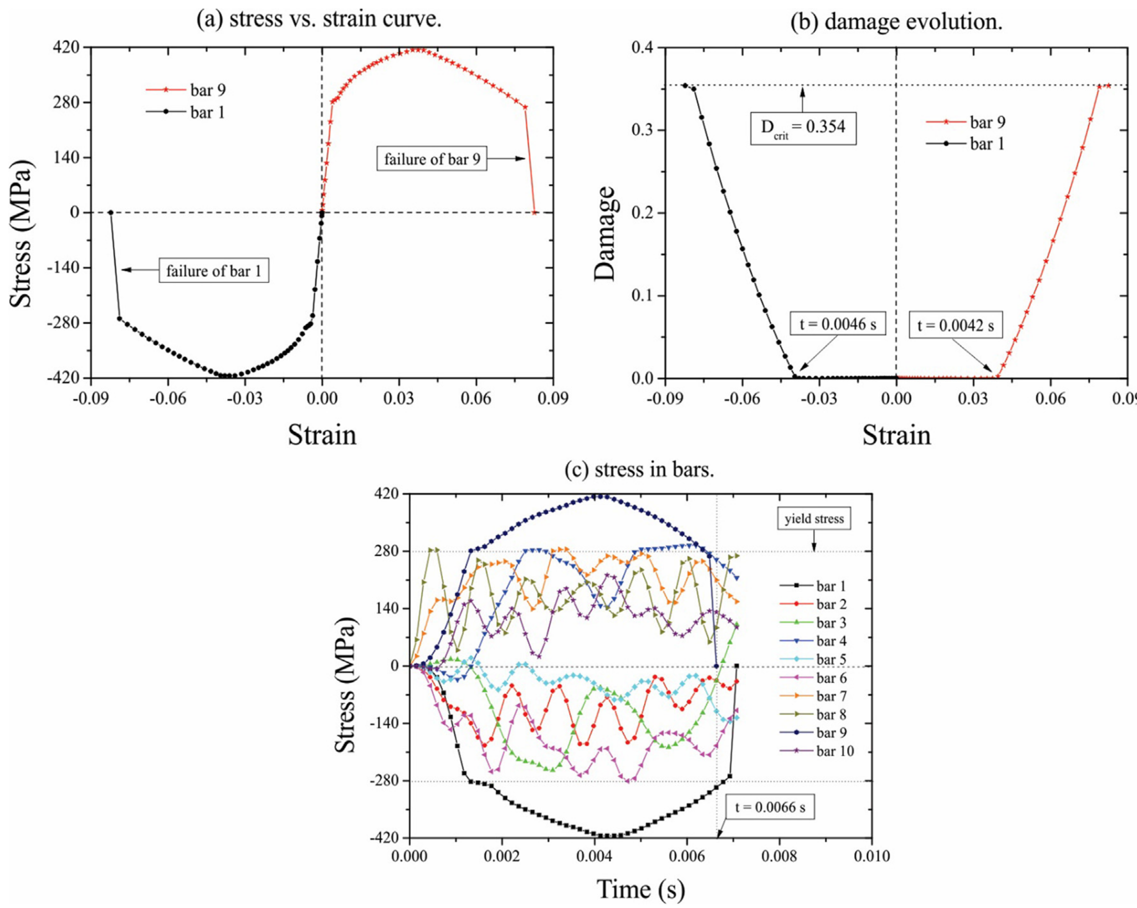

Fig. 11. (a) stress vs. strain curves for bars 1 and 9; (b) damage evolution in bars 1 and 9; and (c) stress vs. time curves for bars 1 to 10.

$\varepsilon^{p}_{\text{ln},d} = 3.33x10^{-4}$ and D_{crit} = 0.50. Angular natural frequency is 5.4751 Hz. Newmark parameters are β_n = 0.25 and γ_n = 0.50. Time step is Δt = 0.01 s. Results are compared with solutions provided by the ANSYS® software. In this example, the joint effects of material and geometrical nonlinearities can be appreciated.

Fig. 13 presents the nonlinear static response of the shallow arch truss, for a force applied in node 1 equal to −140 kN, same as the amplitude of the dynamic external force to be applied in the sequence. An excellent agreement in observed

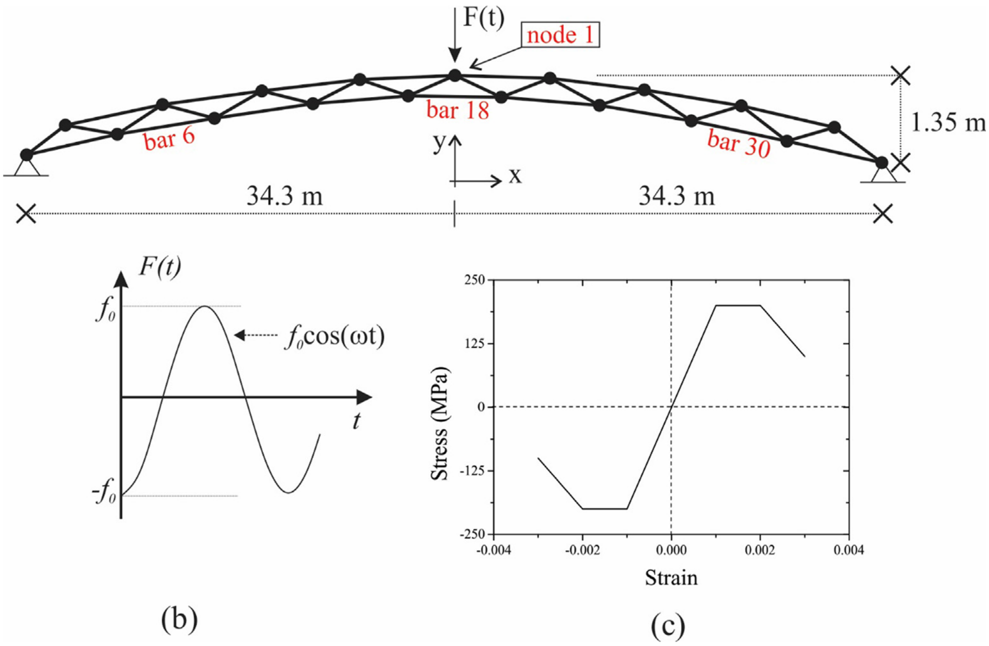

Fig. 12. Input data: (a) geometry of shallow arch; (b) harmonic loading; and (c) constitutive law of the material.

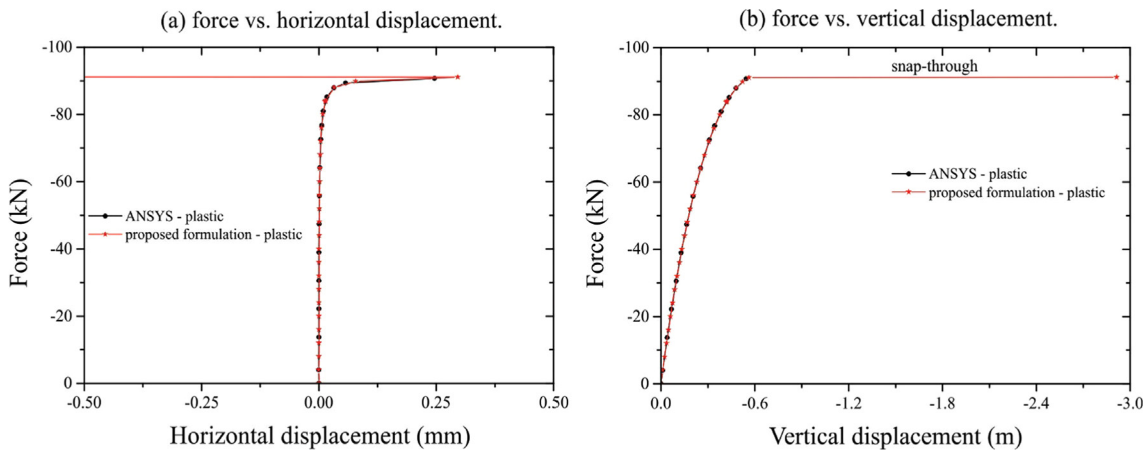

Fig. 13. Nonlinear static response of the shallow arch truss: (a) force vs. horizontal displacement curve; and (b) force vs. vertical displacement curve.

between the proposed plastic solution and results of the ANSYS software. Note that the limit point for snap-through force is equal to F_{lim} = 91 KN, as illustrated in Fig. 13(b). F_{lim} is the maximum force that the shallow truss arch resists, in a stable regime of static equilibrium, considering the effects of material and geometrical nonlinearity. For this analysis, the damage response is equal to the plastic response, because the snap-through occurs before the material reaches the softening regime.

Newmark time integration is unconditionally stable for linear analysis. However, in nonlinear analysis the numerical stability of this integration algorithm is ensured by using a small time step. Fig. 14 presents the convergence analysis of the time step. As observed in Fig. 14, the Newmark time integration is stable with $\Delta t \leq 0.01$ s. Experience has shown that a $\Delta t < T_n/20$ (where T_n is the natural period), is usually sufficient to maintain numerical stability in nonlinear analysis. Thus, the following analyses are made considering Δt = 0.01 s.

Fig. 15 shows the nonlinear dynamic response of the shallow arch truss, in terms of displacements versus time. Remark that the results obtained are in good agreement with software ANSYS®. Note that the damage solution leads to greater vertical displacements than the plastic solution, according to Fig. 15(b). This occurs because the damage solution takes into account the mechanical degradation process, which decreases material stiffness.

Fig. 16 presents the force vs. displacement curve for the shallow truss arch, under harmonic loading. As observed, there is a excellent agreement between the implemented plastic solution and the plastic solution by ANSYS® software. In the

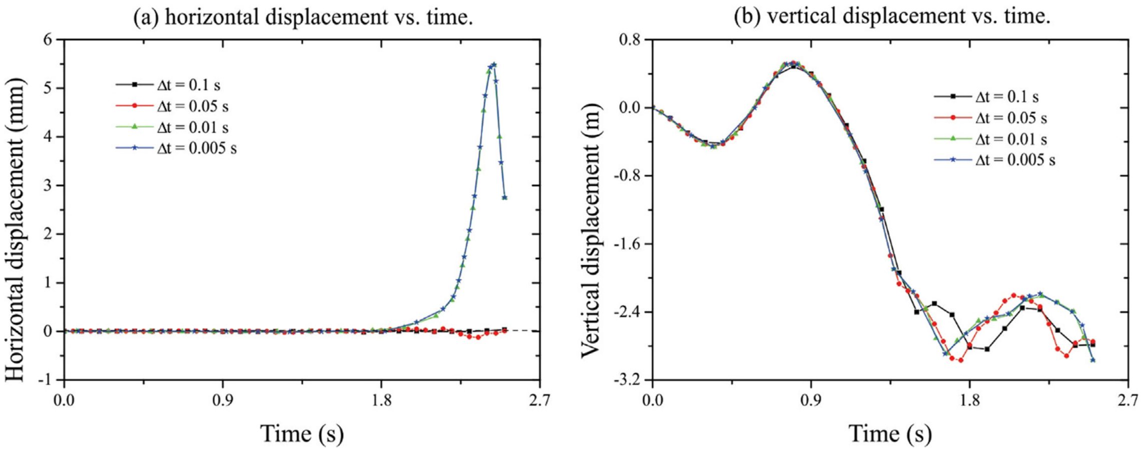

Fig. 14. Convergence analysis for integration time step, displacement time histories in direction: (a) horizontal (X); and (b) vertical (Y).

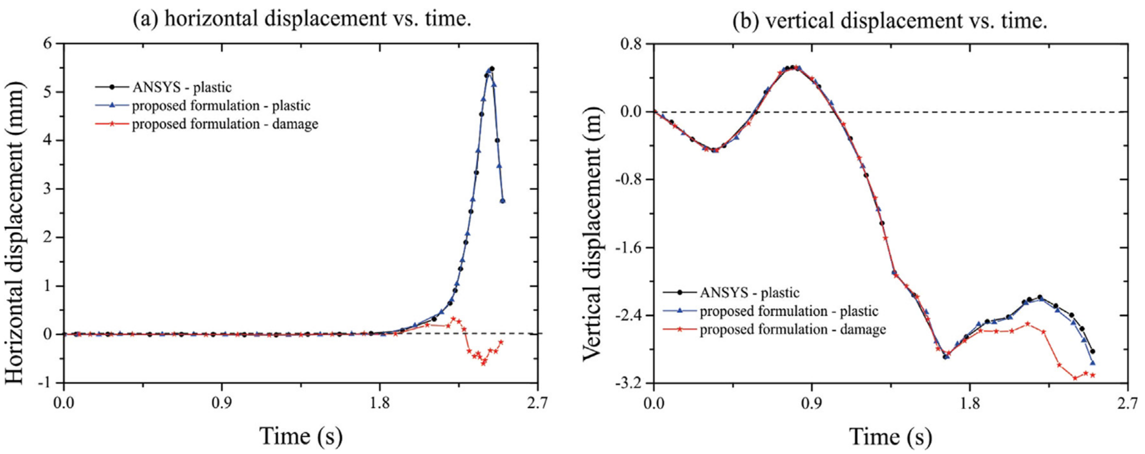

Fig. 15. Nonlinear dynamic response of the shallow arch truss: displacement time histories in direction: (a) horizontal (X); and (b) vertical (Y).

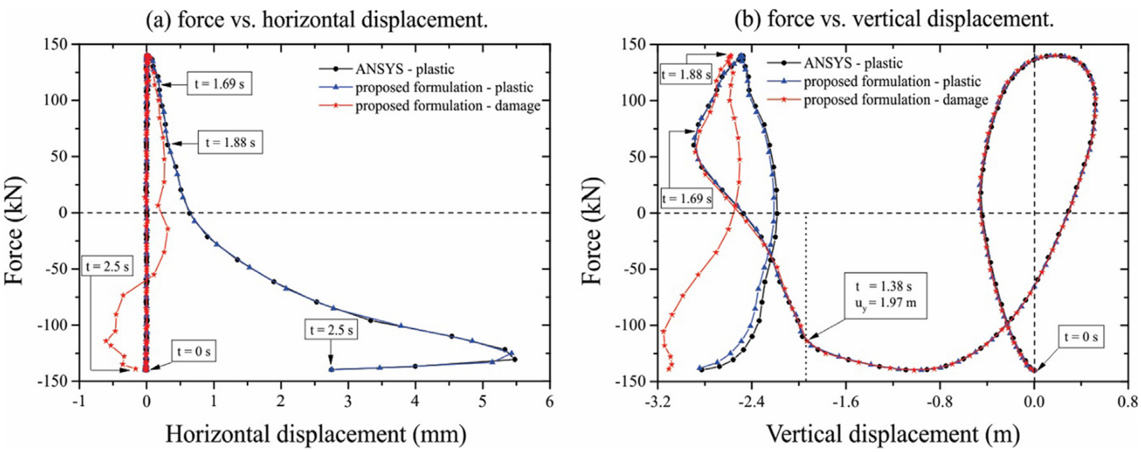

Fig. 16. Nonlinear dynamic response of the shallow arch truss: (a) force vs. horizontal displacement curve; and (b) force vs. vertical displacement curve.

dynamic solution, snap-through does not occur when F_{lim} is reached, in the first positive cycle, since: a) the rate of loading leads to increase in stiffness, and b) energy is dissipated by damping. Until time t = 1.38 s, the material is in the elastic regime, which results in a greater area enclosed by the force vs. vertical displacement curve, as illustrated in Fig. 16(b). There is no energy dissipation due to plastic strains, nor to mechanical degradation. For t > 1.38 s, plastification of the bars is initiated, especially bar 18. At this point (t = 1.38 s), there is an abrupt change in the force vs. vertical displacement curve, according to Fig. 16(b). Also, in the plastic regime, the area enclosed by the force vs. vertical displacement curve becomes smaller, due to energy dissipation by plastic strains.

Concerning failure path of the nonlinear dynamic solution with damage, by t = 1.69 s, bar 18 reaches the initial damage threshold, resulting in loss of local stiffness. By t = 1.88 s, bar 18 reaches the critical damage, while bars 6 and 30 pass the initial degradation limiar, leading to sudden loss of stiffness of the shallow arch truss. Remark that the area enclosed by the force vs. vertical displacement curve is even smaller than the curve of the plastic regime because, due to energy dissipation in plastic strains and in mechanical degradation. The ANSYS® solution does not address the nonlinear damage dynamic response, as it does not contain an equivalent model.

4. Numerical examples: failure paths under dynamic loading

This section demonstrates the accuracy of the proposed formulation in simulating the failure paths of truss structures under dynamic loading. To simulate local failure of individual bars, two approaches can be used: *(i)* removal of bars that reach the critical damage; or *(ii)* provide Young's modulus approximately equal to zero for the bars that reach critical damage. In this paper, the second approach is employed, as it avoids the need to re-mesh the structure, during the iterative process of finding the nonlinear response.

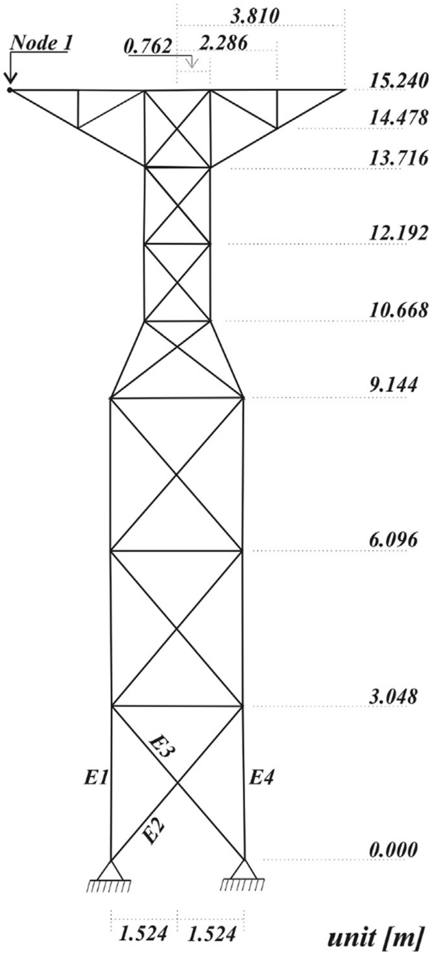

Fig. 17. Geometry of the studied truss tower.

4.1. Forty-seven member 2D truss tower under earthquake loading

This example illustrates the mechanical performance of a forty-seven member 2D truss tower subject to seismic loading, in which the mechanical behavior of truss members are assumed either as elastic, elastoplastic or elastoplastic with damage. Fig. 17 presents the geometry input data of the tower. The tower is subject to the El-Centro earthquake (1940), with the displacement spectrum taken from [27]. The element cross-section areas are A_0 = 100 mm^2; damping ratio is equal to ξ = 0.02 and the time step is Δt = 0.01 s. Newmark parameters are β_n = 0.25 and γ_n = 0.50. The material and damage parameters considered are the same as those of example 3.2.2. The angular frequency is equal to ω_n = 45.67 Hz.

Fig. 18 illustrates the first three vibration modes of the tower. Notice that the first and second modes are flexural, whereas the third is tensile. The first vibration mode and the damping ratio enable construction of the damping matrix, according to Eq. (18).

Fig. 19(a) shows the horizontal displacement vs. time curves for the top left node of the tower (node 1, as shown in Fig. 17), for the three modeling cases: elastic, elastoplastic and elastoplastic with damage. As expected, a large difference can be observed between the responses, in which larger displacements occur in the elastic case. The plastic analysis leads to reduced values of displacements, because of the yielding of members E1, E2, E3 and E4 at the bottom of the tower (see Fig. 17). The elastoplastic with damage condition shows much smaller displacements, because of damage accumulation at members E2 and E3. These elements reach the critical damage at 0.56 s, which triggers the complete collapse of the tower due to hypostatic condition, as detailed below.

Fig. 19(b) illustrates the damage evolution for members E2 and E3, whereas Fig. 19(c) shows the time-history of plastic strains for the same elements. Yielding of these elements starts at 0.45 s. At the time t = 0.47 s, these members reach the initial damage threshold: mechanical degradation starts, with a damage value equal to 0.046. In the time interval of 0.48 s to 0.49 s, elastic unloading occurs, as demonstrated by the earthquake displacement detail in Fig. 19(d). This unloading triggers reversion of stresses, to tensile in bar E2 and compression in bar E3. Then, as the yielding criterion has not been reached between points 2 and 3, this behavior leads to a constant value for total plastic strains (Fig. 19(c)) and damage (Fig. 19(b)). From point 3, the plastic strains evolve until elements E2 and E3 reach the critical damage, which leads to the full collapse of the tower. It is worth stressing that the real mechanical behavior modeling of this tower requires the comprehensive ductile damage model presented herein. Geometrical nonlinear analysis is far from representing structural behavior. Geometrical and material non-linear analyses (with plasticity only) do not represent accurately the mechanical degradations at certain strain levels. The comprehensive ductile damage model developed herein correctly captures the complete failure paths of truss structures subject to dynamic loading.

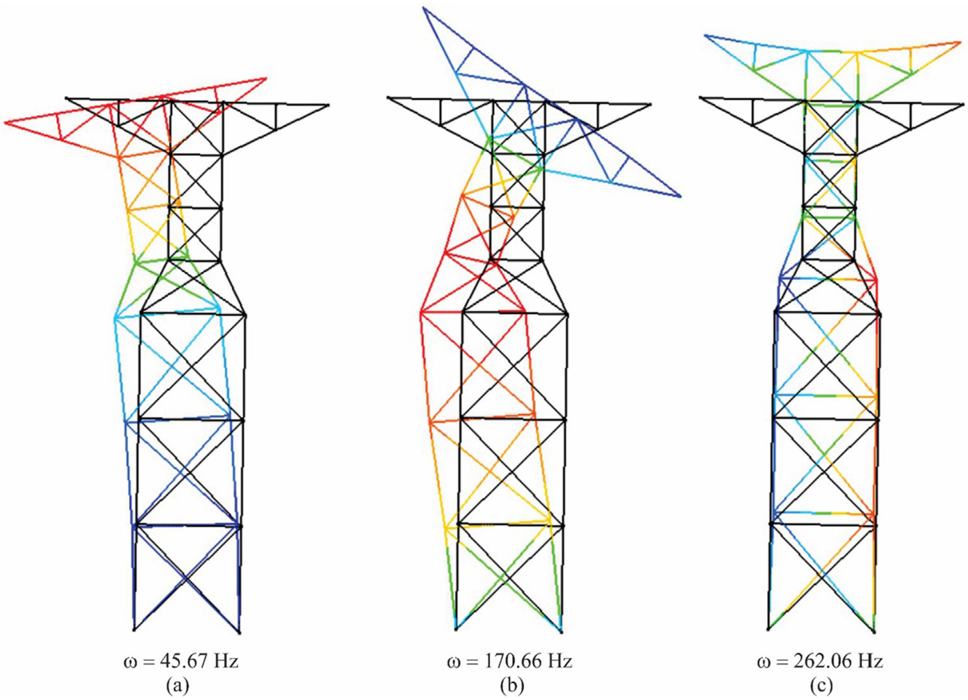

Fig. 18. Tower vibration modes: (a) first; (b) second; and (c) third.

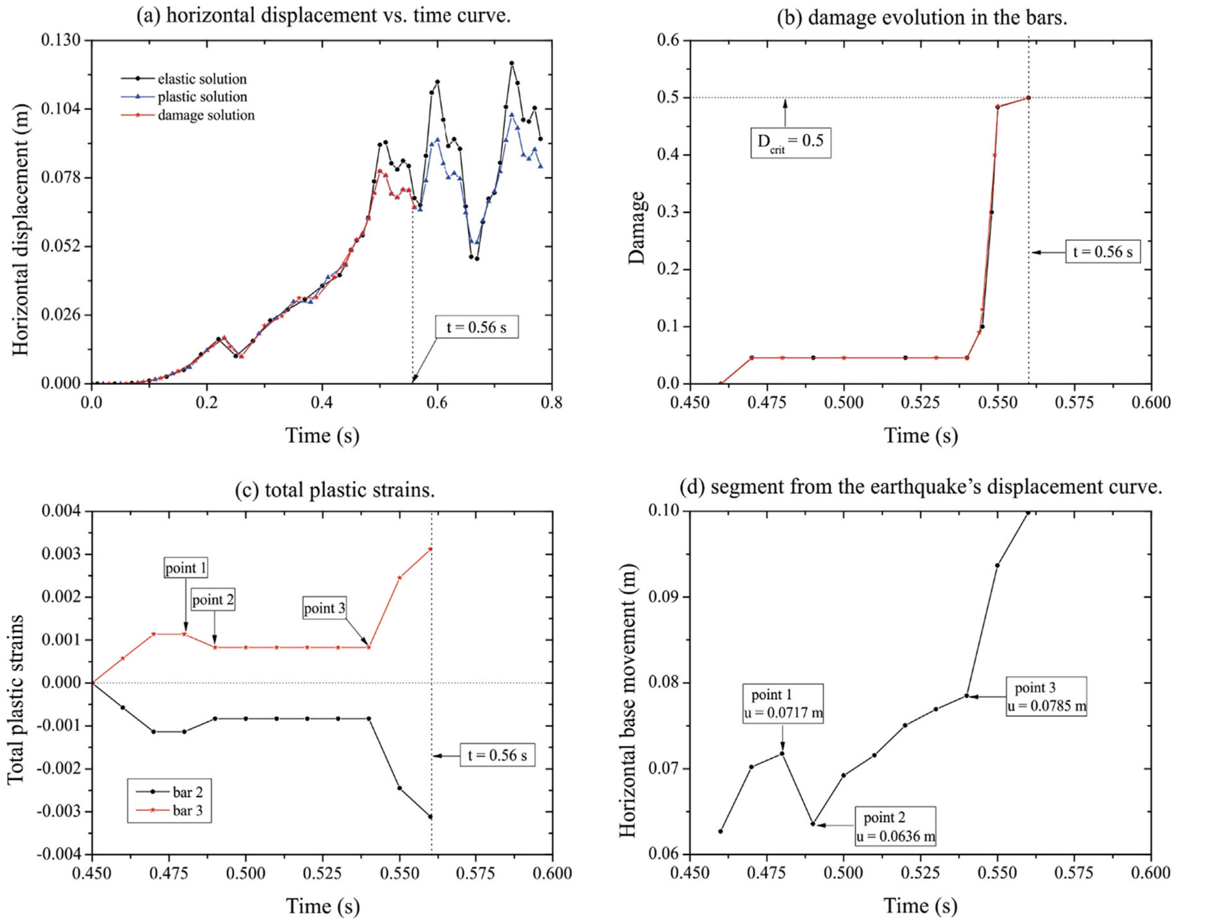

Fig. 19. (a) horizontal displacement vs. time curve for node 1; (b) damage evolution in the bars; (c) total plastic strains in the bars and (d) segment from the earthquake's displacement curve.

4.2. Geodesic truss dome under impulse loading

Impulse loadings have a very short duration and are caused by explosions, shock, failure of structural elements, support failure, etc. [27]. Progressive collapse can be initiated by explosive events leading to impulse loading [39]. Fig. 20 shows a geodesic truss dome, which is submitted to a symmetric triangular impulse load of duration t_d. The forcing function is expressed as [27]:

$$\delta(t) = \begin{cases} \frac{2\delta_0 t}{t_d} \text{ for } t \geqslant 0 \\ \frac{2\delta_0 (t_d - t)}{t_d} \text{ for } t > \frac{t_d}{2} \\ 0 \text{ for } t > t_d \end{cases} \tag{46}$$

where δ_0 = -0.082 m (amplitude of impulse load) and t_d = 0.0024 s (duration of impulse load).

The bar cross-section areas are A_0 = 7850 mm^2; damping ratio is equal to ξ = 0.05; time step is $\Delta t = 10^{-5}$ s and the natural angular frequency is equal to ω_n = 1743.5 Hz. Newmark parameters are β_n = 0.25 and γ_n = 0.50. Fig. 20(c) presents the stress vs. strain curve of the material. The material parameters are: $\aleph$ = 200 GPa; τ_y = 200 MPa and ρ_0 = 7580 Kg/m^3. Damage parameters are:$\alpha_1^p = 0$; $\alpha_2^p = 73.306$; $\alpha_3^p = 0$; $\varepsilon_{\text{ln},d}^p = 2.64x10^{-3}$ and D_{crit} = 0.121.

Fig. 21 illustrates the nonlinear static responses of the geodesic trus dome for $\delta(t) = \delta_0$. The displacement is applied in one hundred and twenty load steps. As observed in Fig. 21(a)-(b), the nonlinear elastic static solution is far from the actual response for this structure. Note that the slope of the curves of the elastic response is larger than the plastic response, since the elastic solution does not consider the loss of stiffness caused by plastic strains, as illustrated in Fig. 21(a)-(b). For an elastic limit displacement of $\delta_{\text{lim,e}} = -8.2$ mm, the snap-through elastic force is $F_{\text{lim,e}} = -490.9$ kN. At this point, the determinant of the Hessian matrix is null; consequently, the equilibrium is neutral. Between displacements of -8.2 and -44 mm, the Hes-

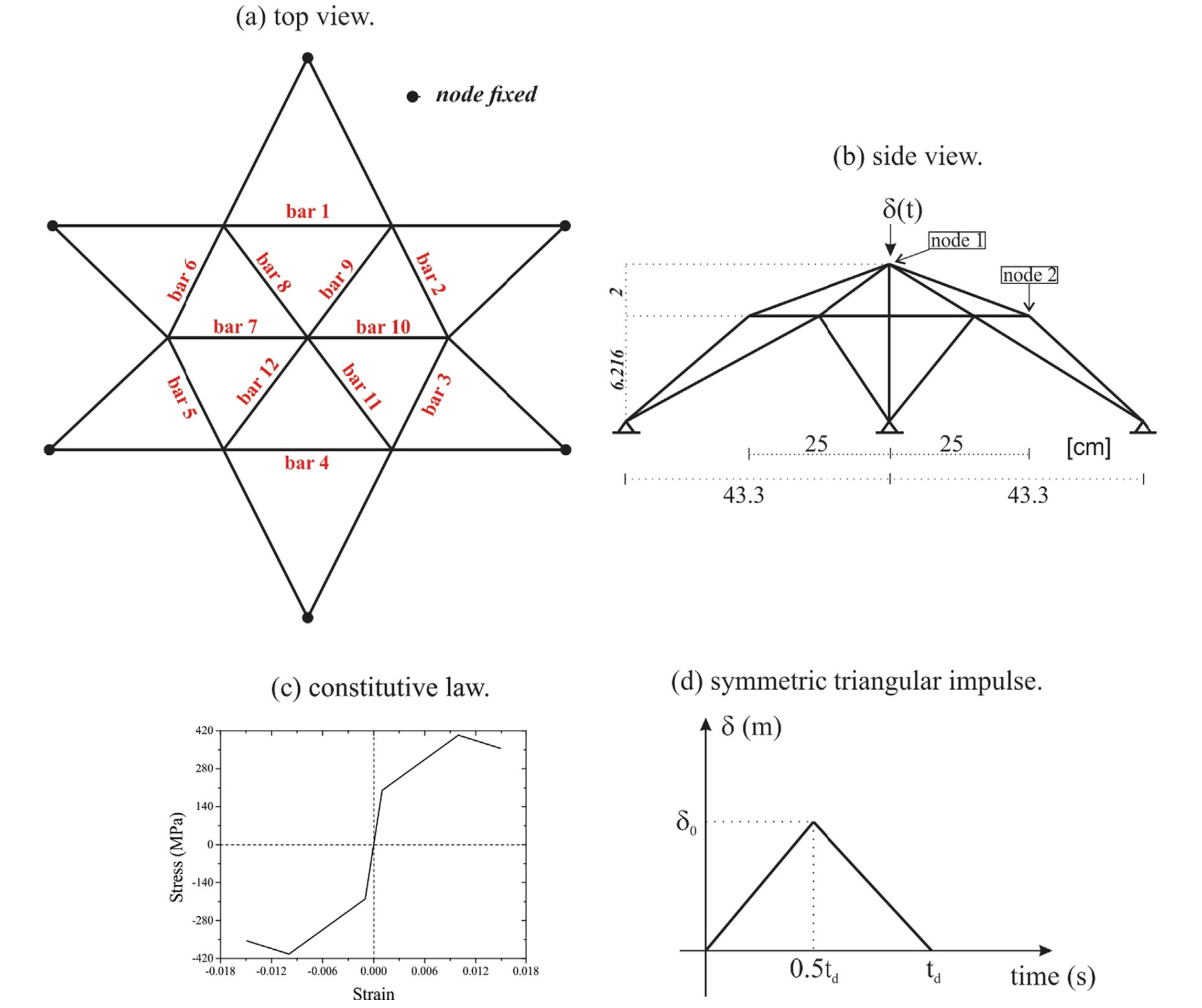

Fig. 20. Geodesic truss dome: (a) top view; (b) side view; (c) constitutive law of the material and (d) symmetric triangular impulse load.

sian matrix is negative (unstable regime); hence, convergence criterion in force cannot be used. Results present in Fig. 21 were obtained with a convergence criterion based on positions (Eq. (35)), with tolerance equal to 10^{-6}.

Regarding the nonlinear plastic static solution, remark the reduction in stiffness due to the appearance of the plastic strains, as illustrated in Fig. 21(a)-(b). Also, the snap-through plastic force ($F_{lim,p} = -476.4$ kN) and plastic limit displacement ($\delta_{lim,p} = -6.56$ mm) are smaller for the plastic response, compared to the elastic case (see point 1 in Fig. 21(a)). As observed in Fig. 21(d), when the bars 2, 3, 5 and 6 reach the ultimate stress, they yield under constant stress levels of -404 MPa. The softening behavior is not captured by the plastic solution. On the other hand, the comprehensive ductile-damage FLHB model yields very consistent results. At point 2 in Fig. 21(a), bars 2, 3, 5 and 6 reach the initial damage threshold, resulting in loss of local stiffness and damage evolution on these bars. The second stiffness loss change (point 3) occurs when the bars 1 and 4 reach the initital damage threshold. Mechanical degradation process remain until the bars 2, 3, 5 and 6 reach critical damage, leading to complete collapse of the geodesic truss dome.

Fig. 22 shows the nonlinear dynamic responses of the geodesic truss dome. In nonlinear dynamic solution, the snap-through force is greater than in the static solution. Considering the plastic material analysis, the increase in snap-through force is of 26.8%, with respect to the static solution. Nonetheless, limit displacement is smaller for the dynamic response, since stiffness increases with the rate of loading.

As observed in Fig. 22(a)-(b), the developed comprehensive ductile-damage FLHB model captures local failure of bars 7 to 12, which occurs when the critical damage value is reached. As a consequence, the ductile-damage solution is very different than the purely plastic solution, which does not capture softening behavior. Importantly, in the dynamic analysis, the dome

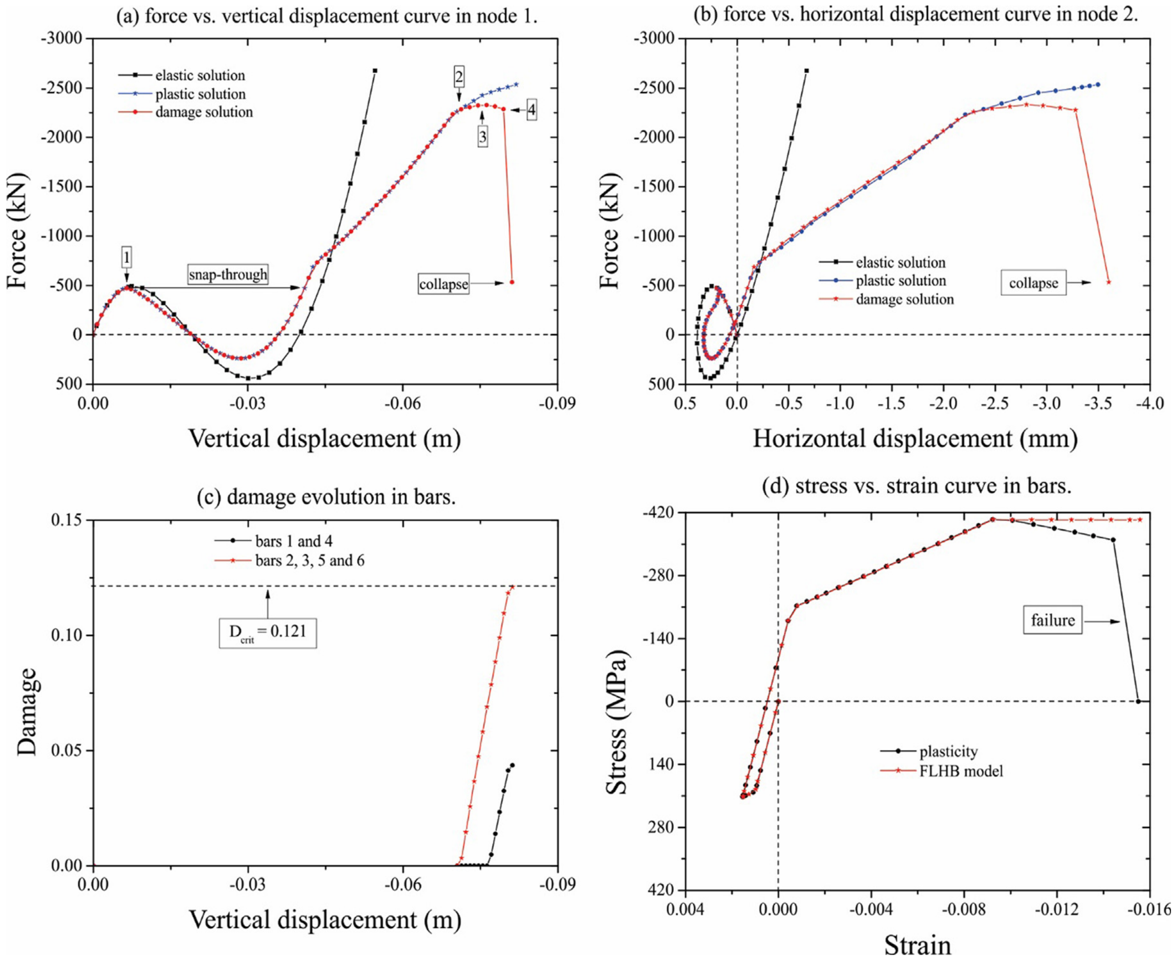

Fig. 21. Nonlinear static solutions of the geodesic truss dome for δ(t) = δ_0: (a) force vs. vertical displacements for node 1; (b) force vs. horizontal displacements for node 2; (c) damage evolution in bars and (d) stress vs. strain curve of bars 2, 3, 5 and 6.

collapses due to failure of bars 7 to 12, whereas in the static analysis, bars 1 to 6 fail first. This points out to the importance of considering dynamic solutions in failure path analysis.

Addressing some details of the plastic solution failure path, note that when the material reaches ultimate stress, the bars yields under the constant stress of 404 MPa, until the strain of 0.01974. For time $t \geq 0.00120$ s, the impulse load starts to decrease, and elastic unloading occurs, until the strain level of 0.01547 (at t = 0.00126 s), as illustrated in Fig. 22(d). Between times 0.00126 s and t = 0.0024 s, the elastic range remains unchanged since strain hardening is equal to zero. Between times 0.00198 and 0.0024 s occurs the second unloading.

Failure path of the nonlinear dynamic response with the FLHB model shows that, at time t = 0.00091 s (vertical displacement of −62.18 mm), the bars 7 to 12 reach the initial damage threshold, resulting in loss of local stiffness, as illustrated in Fig. 22(a). The mechanical degradation process continues until these bars reach the critical damage, which occurs for a vertical displacement of −71.75 mm (t = 0.00106 s); this leads to the complete collapse of the geodesic truss dome. Note that, in the dynamic response, collapse occurs at a displacement level smaller than that of the static response. Moreover, the collapse of the geodesic truss dome occurred with distinct failure modes.

4.3. Efficiency evaluation

The formulation proposed herein for the dynamic analysis of truss structures leads to simple mathematical formalism, easy numerical implementation and low computational cost. This last claim is evaluated by an analysis of computer processing times, as reported in Table 1. Numerical solutions were computed on an Intel Core i7-8550U processor, with clock speed of 1866 MHz. As observed in Table 1, the nonlinear dynamic solutions reported in this paper were obtained within very small computation times.

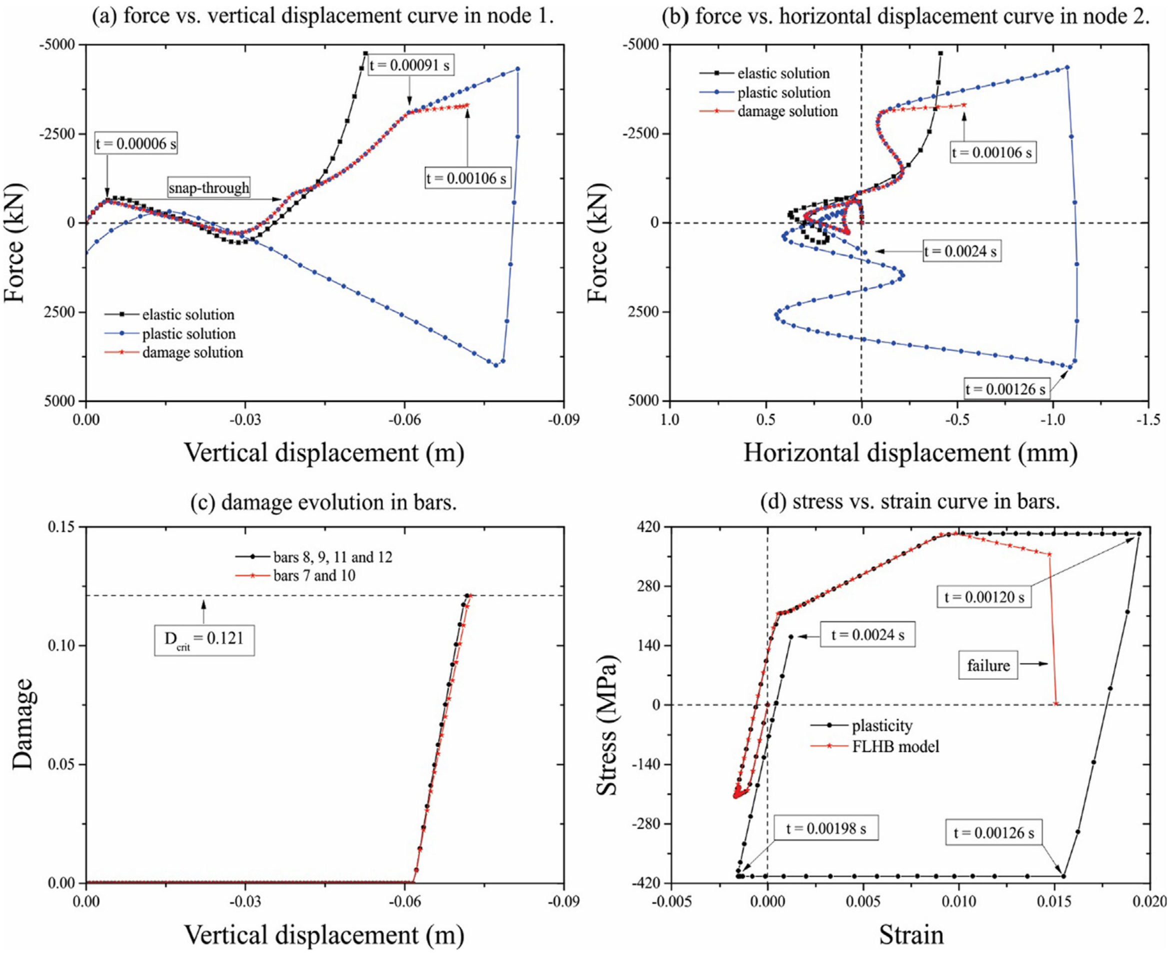

Fig. 22. Nonlinear dynamic solution of the geodesic truss dome: (a) force vs. vertical displacement curve in node 1; (b) force vs. horizontal displacement curve in node 2; (c) damage evolution in bars and (d) stress vs. strain curve in bars 8, 9, 11 and 12.

Table 1
Processing time of the analyses.

Section	Example	Analysis	Processing time (s)
3.1.1	Response to a step load	Elastic	0.04687
		Plastic	0.06250
		Damage	0.07812
3.1.2	Response to forced harmonic loading	Elastic	0.03125
		Plastic	0.09375
		Damage	0.10938
3.2.1	Two-bay cantilever truss	Plastic	0.01562
		Damage	0.03125
3.2.2	Shallow truss arch	Plastic	0.10938
		Damage	0.21875
4.1	Forty-seven member 2D truss tower under earthquake loading	Elastic	0.10938
		Plastic	0.14060
		Damage	0.15625
4.2	Geodesic truss dome under impulse loading	Elastic	0.12500
		Plastic	0.20310
		Damage	0.32810

5. Concluding remarks

In this paper, novel benchmark solutions were proposed for nonlinear dynamic progressive collapse analysis of truss structures. These solutions were computed with a comprehensive ductile damage model proposed elsewhere, but extended herein to dynamic analysis of trusses. The formulation uses nodal positions, instead of displacements, for writing the mechanical energy functional. A logarithmic strain measure is employed for a geometrically exact description of truss displacements. The simple mathematical formalism does not require rotation of coordinate systems, and leads to easy numerical implementation and low computational cost.

Non-linear material modelling associates material damage accumulation to the hydrostatic component of plastic strains. Material hardening and softening are readily captured, as well as material degradation due to porority accumulation. Damage accumulates in members until the critical damage hypothesized by Lemaitre is reached, avoiding material degeneration under large deformations. Thus, the numerical progressive collapse analysis can be carried forward, with failed members transferring their internal forces to adjacent members, until local or global loss of equilibrium.

Benchmark problems were taken from the literature. Observed truss behaviors included yielding, inelastic snap-through, unloading and reloading. Excellent agreement was observed for the elastic and elasto-plastic responses provided in the literature. However, significantly different responses were observed when the FLHB plastic-damage solution was computed, revealing the importance of considering material degradation in numerical analyses. The plastic-damage solutions could not be compared with the literature, as they are a novel contribution of this manuscript. The presented set of results is proposed as the new benchmarks to which non-linear plastic-damage responses of truss structures under dynamic loading should be compared.

CRediT authorship contribution statement

Túlio R.C. Felipe: Methodology, Validation, Formal analysis, Resources, Writing - original draft, Writing - review & editing. **André T. Beck:** Conceptualization, Supervision, Project administration, Funding acquisition, Writing - review & editing.

Declaration of Competing Interest

The authors declare that they have no known competing financial interests or personal relationships that could have appeared to influence the work reported in this paper.

Acknowledgments

The authors acknowledge funding of this research project by Brazilian agencies CAPES (Brazilian Higher Education Council – Finance Code 001), CNPq (Brazilian National Council for Research, grant n. 309107/2020-2) and FAPESP (São Paulo State Research Foundation, grant n. 2017/01243-5).

Appendix A. Supplementary data

Supplementary data to this article can be found online at https://doi.org/10.13140/RG.2.2.11640.16647.

References

[1] S. Szyniszewski, T. Krauthammer, Energy flow in progressive collapse of steel framed buildings, Eng. Struct. 42 (2012) 142–153.
[2] B. Asgarian, F.H. Rezvani, Progressive collapse analysis of concentrically braced frames through EPCA algorithm, J. Constr. Steel Res. 70 (2012) 127–136.
[3] M. Liu, Progressive collapse design of seismic steel frames using structural optimization, J. Constr. Steel Res. 67 (2011) 322–332.
[4] H.S. Kim, J. Kim, D.W. An, Development of integrated system for progressive collapse analysis of building structures considering dynamic effects, Adv. Eng. Softw. 40 (2009) 1–8.
[5] J.W. Smith, Structural robustness analysis and the fast fracture analogy, Struct. Eng. Int. 16 (2006) 118–132.
[6] S. Gerasimidis, J. Sideri, A new partial-distributed damage method for progressive collapse analysis of steel frames, J. Constr. Steel Res. 119 (2016) 233–245.
[7] G. Kaewkulchai, E. Williamson, Beam element formulation and solution procedure for dynamic progressive collapse analysis, Comput. Struct. 82 (2004) 639–651.
[8] J.M. Adam, F. Parisi, J. Sagaseta, X. Lu, Research and practice on progressive collapse and robustness of building structures in the 21st century, Eng. Struct. 173 (2019) 122–149.
[9] A.K. Noor, J.M. Peters, Nonlinear dynamic analysis of space trusses, Comput. Methods Appl. Mech. Eng. 21 (1980) 131–151.
[10] K. Zhu, F.G.A. Al-Bermani, S. Kitipornchai, Nonlinear dynamic analysis of lattice structures, Comput. Struct. 52 (1994) 9–15.
[11] R.B. Malla, P. Agarwal, R. Ahmad, Dynamic analysis methodology for progressive failure of truss structures considering inelastic postbuckling cyclic member behavior, Eng. Struct. 33 (2011) 1503–1513.
[12] H.T. Thai, S.E. Kim, Nonlinear inelastic time-history analysis of truss structures, J. Constr. Steel Res. 67 (2011) 1966–1972.
[13] T.R.C. Felipe, E.D. Leonel, V.G. Haach, A.T. Beck, A comprehensive ductile damage model for 3D truss structures, Int. J. Non-Linear Mech. 112 (2019) 13–24.
[14] R. Carrazedo, H.B. Coda, Triangular based prismatic finite element for the analysis of orthotropic laminated beams, plates and shells, Compos. Struct. 168 (2017) 234–246, https://doi.org/10.1016/j.compstruct.2017.02.027.
[15] T.M. Siqueira, H.B. Coda, Total Lagrangian FEM formulation for nonlinear dynamics of sliding connections in viscoelastic plane structures and mechanisms, Finite Elem. Anal. Des. 129 (2017) 63–77, https://doi.org/10.1016/j.finel.2016.12.005.
[16] H.B. Coda, R.R. Paccola, A total-Lagrangian position-based FEM applied to physical and geometrical nonlinear dynamics of plane frames including semi-rigid connections and progressive collapse, Finite Elem. Anal. Des. 91 (2014) 1–15.
[17] D.L. Henann, L. Anand, A large deformation theory for rate-dependent elastic-plastic materials with combined isotropic and kinematic hardening, Int. J. Plast. 25 (2009) 1833–1878, https://doi.org/10.1016/j.ijplas.2008.11.008.

[18] C. García Garino, J. Oliver, Um modelo constitutivo para el análisis de sólidos elastoplásticos sometidos a grandes deformaciones. Parte I: Formulación teórica y aplicación a metales, Rev. Int. Métodos Numéricos Para Cálculo y Diseño En Ing 11 (1995) 105–123.
[19] S. Nemat-Nasser, On finite deformation elasto-plasticity, Int. J. Solids Struct. 18 (1982) 857–872, https://doi.org/10.1016/0020-7683(82)90070-1.
[20] E.H. Lee, Elastic-Plastic Deformation at Finite Strains, Stanford University, 1968.
[21] J. Lemaitre, R. Desmorat, Engineering Damage Mechanics, Springer, New York, 2005.
[22] J. Simo, T.J. Hughes, Computational Inelasticity, Springer Verlag, New York, 1998.
[23] W.-F. Chen, D.-J. Han, Plasticity for Structural Engineers, Springer Verlag, New York, 1988.
[24] R. Rigobello, H.B. Coda, N.J. Munaiar, A 3D solid-like frame finite element applied to steel structures under high temperatures, Finite Elem. Anal. Des. 91 (2014) 68–83, https://doi.org/10.1016/j.finel.2014.07.005.
[25] A.S. Botta, R.R. Paccola, W.S. Venturini, H.B. Coda, A discussion on volume change in the plastic phase, Commun. Numer. Methods Eng. (2007) 1150–1162.
[26] J. Lemaitre, A Course on Damage Mechanics, Springer Verlag Berlin Heidelberg, New York, 1992.
[27] P. Paultre, Dynamics of Structures, ISTE and Wiley, London, 2011.
[28] J. Argyris, H. Mlejnek, Dynamic of Structures, Elsevier, New York, 1991.
[29] R.W. Clough, J. Penzien, Dynamics of Structures, McGraw-Hill, Tokyo, 1975.
[30] M. Greco, F.A.R. Gesualdo, W.S. Venturini, H.B. Coda, Nonlinear positional formulation for space truss analysis, Finite Elem. Anal. Des. 42 (2006) 1079–1086, https://doi.org/10.1016/j.finel.2006.04.007.
[31] M. Greco, H.B. Coda, Positional FEM formulation for flexible multi-body dynamic analysis, J. Sound Vib. 290 (2006) 1141–1174, https://doi.org/10.1016/j.jsv.2005.05.018.
[32] T. Caughey, M.E. O'Kelly, Classical normal modes in damped linear dynamic systems, J. Appl. Mech. 32 (1965) 583–588.
[33] J.W.S.L. Rayleigh, Theory of Sound, Dover Publications, New York, 1945.
[34] H.B. Coda, R.R. Paccola, A FEM procedure based on positions and unconstrained vectors applied to non-linear dynamic of 3D frames, Finite Elem. Anal. Des. 47 (2011) 319–333, https://doi.org/10.1016/j.finel.2010.11.001.
[35] H.B. Coda, R.R. Paccola, Unconstrained finite element for geometrical nonlinear dynamics of shells, Math. Probl. Eng. 2009 (2009) 1–32.
[36] H.B. Coda, R.R. Paccola, M.D.S.M. Sampaio, Positional description applied to the solution of geometrically non-linear plates and shells, Finite Elem. Anal. Des. 67 (2013) 66–75, https://doi.org/10.1016/j.finel.2012.12.001.
[37] R.W. Ogden, Nonlinear Elastic Deformation, Ellis Horwood, 1984.
[38] N.M. Newmark, A method of computation for structural dynamics, J. Eng. Mech. Div. 85 (1959) 67–94.
[39] B.R. Ellingwood, Mitigating risk from abnormal loads and progressive collapse, J. Perform. Constr. Facil. 20 (2006) 315–323.